Explaining Scales and Statistics of Tropical Precipitation Clusters with a Stochastic Model

FIAZ AHMED AND J. DAVID NEELIN

Department of Atmospheric and Oceanic Sciences, University of California, Los Angeles, Los Angeles, California

(Manuscript received 9 January 2019, in final form 27 June 2019)

ABSTRACT

Precipitation clusters are contiguous raining regions characterized by a precipitation threshold, size, and the total rainfall contained within—termed the cluster power. Tropical observations suggest that the probability distributions of both cluster size and power contain a power-law range (with slope ~ -1.5) bounded by a large-event "cutoff." Events with values beyond the cutoff signify large, powerful clusters and represent extreme events. A two-dimensional stochastic model is introduced to reproduce the observed cluster distributions, including the slope and the cutoff. The model is equipped with coupled moisture and weak temperature gradient (WTG) energy equations, empirically motivated precipitation parameterization, temporally persistent noise, and lateral mixing processes, all of which collectively shape the model cluster distributions. Moisture–radiative feedbacks aid clustering, but excessively strong feedbacks push the model into a self-aggregating regime. The power-law slope is stable in a realistic parameter range. The cutoff is sensitive to multiple model parameters including the stochastic forcing amplitude, the threshold moisture value that triggers precipitation, and the lateral mixing efficiency. Among the candidates for simple analogs of precipitation clustering, percolation models are ruled out as unsatisfactory, but the stochastic branching process proves useful in formulating a neighbor probability metric. This metric measures the average number of nearest neighbors that a precipitating entity can spawn per time interval and captures the cutoff parameter sensitivity for both cluster size and power. The results here suggest that the clustering tendency and the horizontal scale limiting large tropical precipitating systems arise from aggregate effects of multiple moist processes, which are encapsulated in the neighbor probability metric.

1. Introduction

Tropical clouds display a pronounced proclivity to clump together in space. This clumping can extend across multiple spatial scales and lead to coherent precipitating regions or organized convection, spanning scales from $O(1)$ km^2 (a cloudy updraft) to $O(10^5)$ km^2 (a supercluster). Numerous causal pathways can lead to organized convection. Spatial coherence in the dry dynamics—zonal mean ascent (Held and Hou 1980), synoptic vortices (Charney 1947; Eady 1949), tropical waves (Matsuno 1966), etc.—can directly translate to coherence in the ensuing precipitation. Mechanisms internal to moist convection also promote organization. Precipitation-induced cold pools (Zuidema et al. 2017) trigger new convection in the immediate neighborhood ($\sim$100 km) of extant precipitating systems (Tompkins 2001; Feng et al. 2015; Torri et al. 2015). Gravity waves induced by the wiggles in vertical diabatic heating profiles (Mapes 1993; Fovell 2002; Fovell et al. 2006; Tulich and Mapes 2008; Lane and Zhang 2011) favorably modify areas surrounding a precipitating region ($\sim$1000 km). Cloud-permitting models—in certain regimes—allow radiative–convective instabilities to generate spatially coherent regions ($\sim$1000 km) of moist air (Bretherton et al. 2005; Emanuel et al. 2014; Wing et al. 2018), and associated convection. One or several of these mechanisms can act in concert to produce the observed statistics of organized convection.

In this study we seek to understand the primary mechanisms that govern convective organization through the statistics of precipitation clusters, which are defined as spatially contiguous regions precipitating above a specified threshold. These clusters are characterized by their size and the cumulative precipitation they enclose. The latter quantity is presented in units of power and is

Supplemental information related to this paper is available at the Journals Online website: https://doi.org/10.1175/JAS-D-18-0368.s1.

Corresponding author: Fiaz Ahmed, fiaz@ucla.edu

DOI: 10.1175/JAS-D-18-0368.1

therefore termed the ''cluster power.'' In this study we will primarily concern ourselves with the probability density functions (pdfs) of the cluster size and power. These cluster pdfs follow a power law spanning several orders of magnitude before encountering a ''cutoff'' at a large value of size or power (Peters et al. 2009, 2012; Teo et al. 2017; Quinn and Neelin 2017a,b, hereafter QN17a,b). The pdfs for related quantities: cloud sizes (Cahalan and Joseph 1989; Neggers et al. 2003; Wood and Field 2011) and spatiotemporal precipitation clusters (Traxl et al. 2016) appear to belong to the same family of distributions. This family can be approximately described by the function $p(x)$:

$$p(x) \sim x^{-\tau} \exp\left(-\frac{x}{x_L}\right), \tag{1}$$

where x represents either the cluster size or power and $p(x)$ is the pdf of x. Parameters τ and x_L are the slope of the power law and the cutoff, respectively, and together control the incidence of large, powerful clusters. Note that x is free to have any units, but x_L must have the same units as x.

When x specifically denotes the cluster area a or the cluster power c, the following expressions follow from (1):

$$p(a) \sim a^{-\tau} \exp\left(-\frac{a}{a_L}\right),$$

$$p(c) \sim c^{-\tau} \exp\left(-\frac{c}{c_L}\right).$$

Here, a_L and c_L refer to the large-value cutoffs in the distributions of precipitation cluster area and power, respectively. We will hereafter use x_L to collectively refer to both a_L and c_L.

Instantaneous precipitation fields from the Tropical Rainfall Measuring Mission (TRMM) 3B42 (Huffman et al. 2007) yield estimates for the slopes of the cluster size and power pdfs to be $\tau \sim 1.7$ and $\tau \sim 1.5$, respectively (QN17a; Teo et al. 2017). Slightly higher estimates ($\tau \sim 2$) appear for cluster sizes computed using the TRMM Precipitation Radar swaths (Peters et al. 2009, 2012). The mean $\langle x \rangle$ of the distribution (1) depends on both x_L and τ. For the typical observed values of τ ($1 < \tau < 2$), $x_L \gg \langle x \rangle$. For cluster area distributions, a_L can be interpreted as the horizontal scale beyond which the probability of occurrence begins to decrease strongly. This scale corresponds to precipitating systems larger than the typical mesoscale convective system (MCS; Houze 2004), and likely describes spatially connected MCSs, variously referred to as superclusters (Mapes and Houze 1995) or superconvective systems (Chen et al. 1996; Yuan and Houze 2010). In this sense a_L quantifies the degree of organization of a sample of precipitation clusters. To get a sense of the large horizontal scale associated with a_L, consider its typical value $\sim 5 \times 10^5\,\mathrm{km}^2$ (QN17a), which is *100 times* greater than the median values of MCS areas reported in Mohr and Zipser (1996).

Shifts in x_L (both a_L and c_L) therefore highlight changes to the frequency of large and powerful precipitating clusters, and are interpreted as changes to extreme event distributions. For instance, QN17a and QN17b presented evidence of c_L increases in future warmer climates using end-of-century climate model output that translated to greater than a tenfold jump in the frequency of the most powerful precipitating events. This finding is consistent with studies reporting an increasing rain contribution from organized convection in a warming climate (Tan et al. 2015b; Pendergrass et al. 2016). It is imperative to understand factors governing x_L, given the destructiveness of organized convection (Schumacher and Johnson 2005). QN17a and QN17b did not report a significant change in τ with future warming, suggesting that τ is more robust than x_L. The reasons why x_L is more sensitive to parameter changes than τ will be addressed in this study.

The pdfs of rain accumulations (cumulative precipitation across a single event) are similar to cluster power pdfs. Accumulation pdfs are distributed according to (1) with $\tau \sim 1.5$ and exhibit shifts in the accumulation cutoff with future warming (Neelin et al. 2017). Stochastic prototypes (Stechmann and Neelin 2011, 2014) can reproduce the observed accumulation pdfs, and thereby help interpret the anticipated changes with global warming. Similar prototypes for the observed precipitation cluster area and power distributions are, however, absent. A two-dimensional version of the stochastic moisture equation was introduced by Hottovy and Stechmann (2015, hereafter HS15) to explain the observed background spectrum of tropical precipitation. HS15 documented the presence of precipitation clusters in their model and noted a value of $\tau \sim 1.17$ for their cluster size distribution slope, but did not provide details about cluster power pdfs.

Our principal aim in this study is to explain the observed pdfs of cluster size and power, and consequently, identify the physical processes relevant for tropical convective organization. To this end, we present a stochastic model motivated by HS15, and equipped with additional physics relevant for the tropical atmosphere, including dry static energy, water vapor and condensate equations. The deterministic elements of the model follow the thermodynamic equations in the Quasi-Equilibrium Tropical Circulation Model (QTCM; Neelin and Zeng 2000, hereafter NZ00), which are reduced using the weak temperature gradient approximation (WTG; Sobel and Bretherton 2000; Sobel et al. 2001).

TABLE 1. Model parameters as used in the reference run. Parameters used in the perturbation experiments are indicated in the rightmost column, along with the relevant section.

Model parameter	Description	Values	Perturbed (section)
c_p	Heat capacity of dry air	$1004\,\mathrm{J\,kg^{-1}\,K^{-1}}$	No
Δt	Time step	300 s	No
$n_x \times n_y$	Number of model grid points in x and y directions	256×256	No
Δx, Δy	Grid spacing in x and y directions	19.54, 24.97 km	Yes (section 7)
E	Evaporation	$0.14\,\mathrm{mm\,h^{-1}}$	Yes (section 5)
σ	Stochastic forcing amplitude for flux convergence	$6 \times 10^5\,\mathrm{W\,m^{-2}\,s^{1/2}}$	Yes (section 5)
α^{-1}	Moisture adjustment time scale for strong precipitation	2 h	Yes (section 5)
$\alpha_{\mathrm{cond}}^{-1}$	Moisture adjustment time scale for weak precipitation	4 h	Yes (section 5)
$\alpha_{\mathrm{vc}}^{-1}$	Vapor-to-condensate conversion time scale	1 h	Yes (section 5)
D_q	Moisture diffusion coefficient	$7.5 \times 10^4\,\mathrm{m^2\,s^{-1}}$	Yes (section 5)
q_c	Moisture threshold for strong precipitation	60 mm	Yes (section 5)
q_s	Column saturation moisture content	75 mm	Yes (section 5)
τ_{noise}	Characteristic time scale for stochastic flux convergence	2 h	Yes (section 6)
σ_{vort}	Stochastic forcing amplitude for vorticity	$7.17 \times 10^{-2}\,\mathrm{s^{-1/2}}$	No
τ_{vort}	Characteristic time scale for stochastic vorticity	12 h	No
M_{s0}	Reference value of gross dry stability	$3.14 \times 10^4\,\mathrm{kJ\,m^{-2}}$	No
Γ_M	Change in M_s per unit change in q_{cond}	$4.86 \times 10^3\,\mathrm{kJ\,m^{-2}}$	No
M_{qp}	Change in moisture stratification per unit change in q_v	0.53	No
M_{qpc}	Change in condensate stratification per unit change in q_{cond}	−0.98	No

The basic features of model construction are described in section 2. Section 3 contains details of the numerical implementation. Section 4 includes a preliminary look at the precipitation cluster statistics from the model, which bear close correspondence to the observed cluster statistics. The model is then interrogated with parameter perturbation experiments in section 5, which reveal that x_L is sensitive to multiple model parameters. Mechanism denial experiments (section 6) shed further light on the relevant physical pathways controlling x_L. Connections to the site percolation model and its regime of relevance are highlighted in section 7. Section 8 presents analogies between precipitation cluster growth and a class of idealized models called the stochastic branching process. These analogies help devise a neighbor probability metric: the average number of precipitating regions that arise in the neighborhood of an existing precipitating region. Section 8 further shows how that this metric can explain the multiparameter dependence of x_L noted in section 5. Section 9 showcases examples of "self-aggregating" precipitation clusters, akin to those reported in cloud-resolving models (CRMs) under radiative–convective equilibrium (RCE). Section 10 summarizes this work along with its implications.

2. Model description

a. Temperature equation

Our aim here is to construct a minimal complexity model to capture the essential statistics of precipitation clustering. We begin with the vertically integrated temperature equation, which is reduced using the WTG approximation. This reduction transforms our temperature equation to a diagnostic equation for the horizontal divergence:

$$c_p \frac{\partial \overline{T}}{\partial t} + M_s \nabla \cdot \mathbf{v}_1 = L_v (P + Q_{\mathrm{vc}}) + F_s - \xi. \qquad (2)$$

Here, $\overline{T}$ is the domain-averaged, vertically integrated temperature; M_s is the gross dry stability, $\mathbf{v}_1$ is the *horizontally varying* component of horizontal wind, and c_p is the heat capacity of dry air. In contrast to traditional treatments (Sobel et al. 2001), we impose a weaker form of WTG by neglecting horizontal gradients in temperature, but allowing $\overline{T}$ to evolve in time. We demand that there be zero domain-mean divergence, so $\overline{T}$ depends only on the net domain-mean fluxes. The supplement contains a full derivation from the temperature equation leading to (2). Table 1 lists all the model parameters. The column fluxes due to latent heat release are partitioned between convective (or strong) precipitation P and the vapor to condensate conversion Q_{vc}. The net column flux F_s contains the effects of radiative and surface sensible heat fluxes. In our construction, ξ captures the variability arising from absent physics—including stochastic column fluxes and neglected wave dynamics in (2)—and obeys the constraint: $\overline{\xi} = 0$. L_v is a constant that converts P and Q_{vc} from units of millimeters per hour to watts per square meter.

Manipulating (2) leads to an expression for the divergence:

$$\nabla \cdot \mathbf{v}_1 = \frac{L_v(P - \overline{P}) + L_v(Q_{\rm vc} - \overline{Q}_{\rm vc}) + (F_s - \overline{F}_s) - \xi}{M_s}. \tag{3}$$

In (3), the local horizontal divergence is dependent on the local departure from domain-mean, column-integrated fluxes—indicated by overbars—as well as a stochastic component.

The primary governing equation in our model is the vertically integrated water vapor (q_v) budget:

$$\frac{\partial q_v}{\partial t} = (E + R_e - P - Q_{\rm vc}) + M_{qp}(\nabla \cdot \mathbf{v}_1)q_v + M_{qp}\mathbf{v}_1 \cdot \nabla q_v + D_q \nabla^2 q_v, \tag{4}$$

where E and R_e are the surface evaporation of water and the re-evaporation of condensate, respectively. Here, q_v is in units of millimeters. The constant M_{qp} is derived from fixed vertical structures of vertical velocity and water vapor (see the online supplemental material). Note that the full derivation of (4) follows the same steps as in NZ00. Similar to HS15, a horizontal diffusion term with coefficient D_q is present in (4). Diffusion arises naturally in first-order closures of the subgrid scale turbulent fluxes, and emphasizes the nearest neighbor interactions. Such interactions are anticipated to enhance the spatial coherency of the resulting precipitation clusters (Bengtsson et al. 2013; Khouider 2014; Tan et al. 2015a) in the model. Note that diffusion will prove to be an important, albeit simple, representation of the physical mechanisms that encourage convection in the neighborhood of existing convection. These nearest-neighbor effects of diffusion also find use in the related ''coarsening'' model of Craig and Mack (2013).

Observed tropical precipitation clusters contain broad areas of stratiform rain that originate due to the lateral transport of condensate away from the convectively active areas (Houze 1997). This role for stratiform rain led us to anticipate a role for condensate transport in shaping the model precipitation clusters. We therefore include a prognostic equation for vertically integrated mixing ratio of the condensate species $q_{\rm cond}$, complete with advective and diffusive transport:

$$\frac{\partial q_{\rm cond}}{\partial t} = Q_{\rm vc} - P_{\rm cond} + M_{qpc}(\nabla \cdot \mathbf{v}_1)q_{\rm cond} + M_{qpc}\mathbf{v}_1 \cdot \nabla q_{\rm cond} + D_q \nabla^2 q_{\rm cond}, \tag{5}$$

where $q_{\rm cond}$ is in units of millimeters. The constant M_{qpc}—similar to M_{qp}—is derived from assumed vertical structures of the condensate mixing ratio and the vertical velocity (see the online supplement). The cloud condensate species, $q_{\rm cond}$, does not rain out as P; it can be transported laterally and contribute to the weak, large-scale precipitation $P_{\rm cond}$. Note that $Q_{\rm vc}$ contributes to the latent release but $P_{\rm cond}$ does not. In the standard parameter regime, we found that the salient statistics of model precipitation clusters can be captured with the single moisture equation, (4). Sensitivity tests—provided in the online supplement—show that the condensate species only have a quantitative effect on the cluster statistics. We nevertheless retain the condensate equation in our model setup both for the sake of completeness and because we parameterize M_s (shown in the next subsection) based on the amount of condensate in the column. This M_s parameterization plays an important role in preventing runaway column moistening in regimes with large parameter perturbations.

The prognostic equations, (4) and (5), are solved after substituting for the divergence $\nabla \cdot \mathbf{v}_1$ from (3). This substitution introduces a ξ dependence in both the moisture and condensate equations. Note that the stochastic term only enters (4) and (5) through the divergence. Our main governing equations therefore remain conservative; the stochastic term merely redistributes vapor and condensate without introducing additional sources or sinks.

b. Parameterizations

1) Stochastic flux

As is the norm in studies utilizing stochastic methods, we must first decide the spatiotemporal character of our noise field, ξ. The simplest approach here would be to generate a set of random numbers that are completely uncorrelated (or ''white'') in both space and time, as in HS15. Atmospheric random variability that we aim to capture with ξ, however, inherently possesses spatiotemporal autocorrelation. We therefore choose to prescribe temporal correlation to our noise. We will, however, avoid prescribing explicit spatial correlation, as this would be tantamount to controlling the spatial character of the emergent physics. The spatial characteristics of the precipitation field in our model, therefore, emerges from the other physical processes and not the noise itself. We explore the effects of temporally uncorrelated noise in section 6.

Another notable feature of our treatment of the stochastic term is its role in the prognostic equations, (4) and (5), as a multiplicative factor—through the divergence term. This treatment ensures that the noise is magnified in moist environments, and suppressed in dry environments—ensuring that random perturbations do not drive the vapor or condensate values below zero.

We model ξ with a simple Ornstein–Uhlenbeck process (Gardiner 2004), with an autocorrelation time scale τ_{noise}:

$$d\xi = -\tau_{\text{noise}}^{-1}\xi dt + \tau_{\text{noise}}^{-1}\sigma dW(t), \tag{6}$$

where σ is the forcing amplitude of the stochastic term and $dW(t)$ is the derivative of the Wiener process (i.e., Brownian motion).

2) MICROPHYSICS

The model precipitation has two sources: convective precipitation P and the "large-scale" precipitation due to condensate removal P_{cond}. The latent heat release also has two sources: P and the vapor to condensate conversion Q_{vc}. These sources are computed by linearly relaxing the water vapor q_v to threshold values q_c and q_{sat}:

$$P = \alpha(q_v - q_c)H(q_v - q_c), \tag{7}$$

$$Q_{\text{vc}} = \alpha_{\text{vc}}(q_v - q_{\text{sat}})H(q_v - q_{\text{sat}}). \tag{8}$$

Here, H is the Heaviside function such that $H(x) = 1$ for $x > 0$ and $H(x) = 0$ for $x \le 0$, α^{-1} is the relaxation time that controls the convective precipitation strength, q_{sat} is the column-integrated saturation water vapor value, and α_{vc} is the time scale with which water vapor above q_c is converted to condensate (we take $\alpha_{\text{vc}} = 2\alpha$). Note that (7) is a variant of the scheme introduced in Betts (1986) and Betts and Miller (1986).

The large-scale precipitation P_{cond} is parameterized as a fraction α_{cond} of the condensate q_{cond} (we take $\alpha_{\text{cond}} = 0.5\alpha$). The large-scale precipitation P_{cond} can also lose a fraction of its water substance to the unsaturated environment via re-evaporation R_e; this fraction is proportional to the degree of vapor subsaturation. These conditions are represented by

$$P_{\text{cond}} = \alpha_{\text{cond}} q_{\text{cond}} \left[\frac{\min(q_v, q_{\text{sat}})}{q_{\text{sat}}}\right]$$

$$R_e = \alpha_{\text{cond}} q_{\text{cond}} \left[1 - \frac{\min(q_v, q_{\text{sat}})}{q_{\text{sat}}}\right].$$

Note that R_e is nonzero only when condensate is present in a subsaturated environment.

3) GROSS DRY STABILITY M_s

The QTCM vertical structures arise from the assumption that convection responds to large-scale forcing with a single-signed, deep tropospheric temperature adjustment. Moist convective response, however, also involves the two-signed "second-baroclinic mode" heating profile (Mapes 2000; Majda and Shefter 2001) due to the formation of stratiform rain (Houze 1982; Johnson 1984; Schumacher et al. 2004). WTG is a less reasonable approximation for responses involving the second baroclinic mode (Majda et al. 2015). These departures from WTG are, however, assumed to be contained within the stochastic term ξ.

Another relevant role for the second-baroclinic mode in our model is its effect on the "top-heaviness" of the heating profile, which in turn affects M_s and the gross moist stability (Yu et al. 1998; Back and Bretherton 2006; Chou et al. 2013). More specifically, M_s increases with the top-heaviness of the vertical velocity profile, limiting decreases in the gross moist stability which can otherwise lead to runaway column moistening (Raymond et al. 2009). To represent this effect, M_s is allowed to vary with q_{cond} as

$$M_s = M_{s0} + \Gamma_M q_{\text{cond}}, \tag{9}$$

where Γ_M is the coefficient that determines the strength of M_s increase for a unit change in q_{cond}. The dependence on condensate is designed to capture the change in heating structure as stratiform rain contributions increase. The assumed value of Γ_M (Table 1)—along with the vertical structure of condensate (Fig. S1 in the online supplemental material)—translates to ~15% increase in M_s per millimeter of column-integrated condensate. Note that when manipulating (2) to obtain (3), we ignore the spatial variations in M_s due to the q_{cond} dependence in (9).

4) NET COLUMN FLUX F_S

We split F_s in (3) into three components:

$$F_s = F_{\text{ext}} + F_{\text{qre}} + F_{\text{cre}}, \tag{10}$$

where F_{ext} includes contributions to the column flux divergence from the combined radiative effects of the tropospheric and surface temperature, and surface sensible heat transports. In this model we hold F_{ext} fixed in time, but retain the option to allow latitudinal variations that capture the effects of a large-scale, Hadley cell–like circulation (see section 3c). The last two terms on the right-hand side of (1), F_{qre} and F_{cre}, capture the contributions to the column flux divergence from the radiative effects of column-integrated water vapor (CWV) and cloud content, respectively; F_{qre} and F_{cre} are set to zero in the reference version of the run, but are used in sections 6a and 9 to demonstrate the effects of moisture- and cloud–radiative feedbacks.

3. Numerical implementation

The stochastic differential equations, (4) and (5), are solved on a discrete, two-dimensional lattice with periodic boundaries in the x direction and fixed boundaries

in the y direction, with numerics as in the full QTCM (Zeng et al. 2000). Results here use 256 grid points along each direction with grid sizes $\Delta x = 19.54$ km and $\Delta y = 25$ km unless otherwise specified. The domain extent ($\sim$5000 km $\times$ $\sim$6400 km) represents the size of a typical tropical ocean basin. The moisture and velocity variables reside on a staggered Arakawa C grid (Arakawa and Lamb 1977) and evolve with a time step $\Delta t = 300$ s. The time derivatives in the model are numerically solved using the Euler–Maruyama scheme, which is a natural extension of the Euler forward difference scheme for stochastic difference equations. Other model specifications including standard parameter values are detailed in Table 1. Advection by the total wind is modeled using a first-order upwind scheme. Diffusion is modeled using centered differencing in the interior of the domain and one-sided differencing at the boundaries.

a. Generation of the stochastic component ξ

The derivative of the Wiener process [$dW(t)$ in (6)] is white and Gaussian with zero mean, and a variance of Δt. At every time step, a collection of 256 $\times$ 256 uniformly distributed pseudorandom numbers are converted to a Gaussian distribution using the Box–Muller transformation. A two-dimensional field of ξ is then generated from (6) and its domain average is subsequently removed.

b. Generation of the wind field

The advecting wind field, $\mathbf{v}_1$ in (4) and (5) is decomposed into divergent and rotational components:

$$\mathbf{v}_1 = \mathbf{v}_{\text{div}} + \mathbf{v}_{\text{rot}}, \tag{11}$$

where $\mathbf{v}_{\text{div}}$ is calculated by inverting the divergence field in (3), using a Poisson solver with Neumann boundary conditions at the northern and southern boundaries. The Poisson solver computes the velocity potential, whose gradient is the divergent wind. This wind field is subject to the additional constraint of zero flow across the domain boundaries. For the sake of simplicity, we ignore the spatial variations in M_s from (9) in this inversion procedure.

Tropical convective elements are often embedded in large-scale flow features dominated by the vorticity field (Yano et al. 2009). Long-lived vortices and rotational wind effects play an important role in moisture transport between the tropics and the subtropics (e.g., Pritchard and Bretherton 2014). We therefore specify $\mathbf{v}_{\text{rot}}$ in a simple, sensible way to account for its possible effects on precipitation organization. Since our model does not have an explicit rotational wind field, $\mathbf{v}_{\text{rot}}$ is specified as an additional stochastic term. To emphasize the persistent, large-scale nature of the rotational wind field, we construct $\mathbf{v}_{\text{rot}}$ from a stochastic vorticity field that has both spatial correlation and temporal autocorrelation (12 h). Details of this construction are elaborated in the online supplement. The rotational wind $\mathbf{v}_{\text{rot}}$ is not impacted by precipitation, and passively advects vapor and condensate. A complete treatment of rotational wind associated with the divergence field and the effects of planetary rotation can introduce additional complexity (e.g., Nolan et al. 2007; Held and Zhao 2008; Shi and Bretherton 2014; Arnold and Randall 2015; Merlis et al. 2016), and is left for future work.

c. Mock Hadley cell

Tropical precipitation organization can arise from both the internal physics of moist convection as well as external interactions with the large-scale circulation—for example, the Hadley cell. To capture the possible large-scale effects on precipitation clusters, we prescribe a mock Hadley cell [akin to the mock Walker cell in Kuang (2012)]: with a spatially varying flux field that has positive values near the domain center and negative values near the domain boundaries (see Fig. S2). This structure is distinct from the randomly fluctuating component of divergence and is introduced as a meridionally varying external flux term F_{ext} with zero domain mean. We chose the meridional gradients in F_{ext} to be small within $\pm 20°$ latitude, so the cluster dynamics can be easily seen in the near-equatorial region.

The mock Hadley circulation (specified via F_{ext}) and the rotational wind advection (specified via $\mathbf{v}_{\text{rot}}$) prove sufficiently important to warrant their inclusion in the reference run discussed in section 4. We discuss more idealized versions of the model without these features in section 5.

4. Precipitation cluster statistics: Reference run

The model runs discussed in this article have a 1-yr duration. The first 10 days of the simulations include the model spinup time and are excluded from all analyses. The salient features of the cluster distribution statistics are apparent from samples as small as 50 days, but a 1-yr time period is retained to improve sampling. To facilitate useful comparisons with statistics from satellite data, instantaneous precipitation values are output four times daily at 6-h intervals. At every output time step, contiguous model pixels with precipitation rate exceeding a certain threshold are grouped into clusters. The cluster size is defined as the number of pixels in a cluster, multiplied by the area of a single pixel ($dx \times dy \approx 488\,\text{km}^2$). The cluster power, defined as the cumulative precipitation

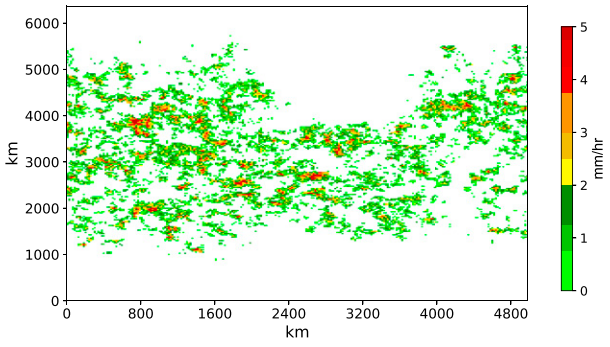

FIG. 1. Snapshot of the precipitation field from a selected time step (day 73, hour 6) in the stochastic model reference run.

within the cluster, has units of gigawatts (GW) as in QN17a and QN17b. The parameters of the reference model run are tabulated in Table 1. Figure 1 is a snapshot (day 73, hour 6) of the precipitation field in the model. The spatial structure of the precipitation field is not unlike images available from satellites (e.g., https://pmm.nasa.gov/gpm/imerg-global-image) over an actively precipitating region of the tropical ocean. The influence of the mock Hadley cell is visible in how the model precipitation avoids the meridional boundaries, preferring to hover near the central latitudes. Much like in real precipitation clusters, swathes of non-precipitating regions surround and highlight the aggregated nature of large precipitating regions. Narrow regions of intense precipitation cores ($>4\,\mathrm{mm\,h^{-1}}$), surrounded by wider, weakly precipitating regions are also visible—quite similar to real precipitating clusters. Note that longitudinal variations in the meridional extent of the precipitating regions in Fig. 1 are in part due to the advection of dry or moist air by the rotational wind (see Fig. S3). The use of a dynamically constrained rotational wind—wherein the vorticity is constrained to have near-zero values in our domain equator, produces the same qualitative results (not shown).

Figures 2a and 2b are the model precipitation cluster size and power distributions, respectively, presented for four different precipitation thresholds, while Figs. 2c and 2d are the observed cluster size and power

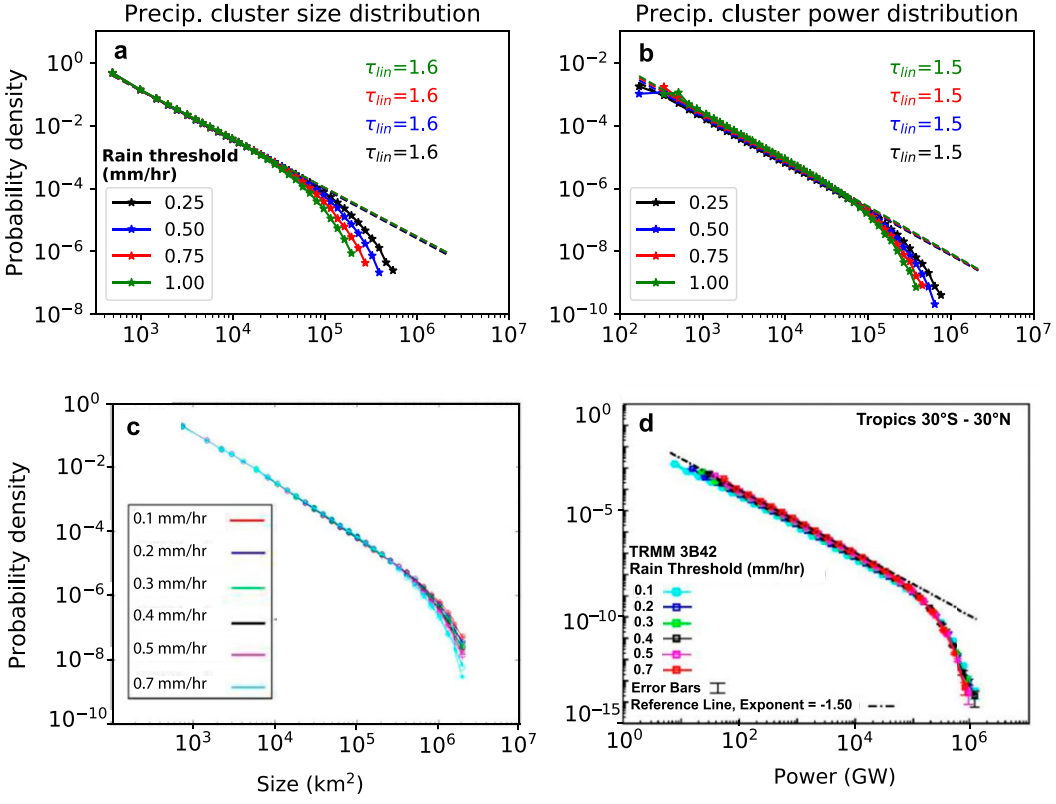

FIG. 2. The pdfs of precipitation (a) cluster size and (b) cluster power from 1-yr-long stochastic model reference run. The pdfs are constructed for different precipitation thresholds, which are indicated by different colors. The slopes of the power law estimated by a linear regression over the power-law range of the curves τ_{lin} for different precipitation thresholds are also indicated. The observed precipitation cluster pdfs from TRMM 3B42 data for (c) size and (d) power from Quinn and Neelin (2017a) are included for comparison. Note the differences in scales of the axes, when comparing the model and observation pdfs.

distributions from TRMM 3B42 data, as published in QN17a. The model cluster pdfs bear a clear resemblance to the observed pdfs. The exponents of the power-law range τ, that is, the slopes in these log–log figures, are computed here using a linear regression over the power-law portion of the curves. For the cluster size pdf in the model, $\tau \sim 1.6$ for different precipitation thresholds, comparable to observational estimates by QN17a (~1.7) and T17 (~1.66). The value of τ for the model cluster power pdf is ~1.5 for different precipitation thresholds, again falling quite close to the estimates from QN17a (~1.5) and T17 (~1.48). The model cluster pdfs, similar to observed, exhibit a noticeable departure from the power law at large values of cluster size and power. The tails of the pdfs beyond the cutoff appear to drop less steeply in the model, than in observations. The cutoff in the model cluster pdfs is also more sensitive to the precipitation threshold, than in the observed pdfs, pointing to discrepancies between the model and observed precipitation distribution. This sensitivity to the precipitation threshold could be a result of our simple convective and microphysics parameterizations (section 2b), though it is worth noting that this sensitivity is a documented feature in even general circulation models (QN17a,b). Generally speaking, the model is able to closely reproduce the statistics of observed tropical precipitation clusters, despite its minimal complexity.

5. Parameter perturbations

As a measure of extreme event occurrence, x_L is an important parameter of the cluster distributions. Understanding the dynamics of x_L shifts can help us anticipate how the distribution of extreme events might change in the future. The sensitivity of both τ and x_L to quantitative perturbations in various model parameters is now considered. We effectively introduce perturbations to five different model parameters: σ, E, q_c, α^{-1}, and D_q. The relaxation times for strong precipitation α^{-1}, vapor to condensate conversion $\alpha_{\mathrm{vc}}^{-1}$ and weak large-scale precipitation $\alpha_{\mathrm{cond}}^{-1}$ are perturbed together, such that $\alpha_{\mathrm{cond}}^{-1} = 2\alpha^{-1}$ and $\alpha_{\mathrm{vc}}^{-1} = 0.5\alpha^{-1}$; q_c and q_{sat}, the threshold values for precipitation and vapor saturation, respectively, are perturbed together such that $q_{\mathrm{sat}} = 1.25q_c$. This parameter set was chosen to gauge the robustness of the cluster pdfs to apparently important free parameters in the model. We conduct these perturbation experiments—analogously to perturbed physics ensembles with climate models—to ask which model parameters show the greatest impact on the cluster pdfs, setting the stage to ask why they do so. The effects of entirely excising particular physical pathways such as lateral mixing or moisture convergence–latent heating coupling are explored in section 6.

The model runs for parameter perturbations are performed in a more idealized setting, without the mock Hadley cell and the rotational wind advection, to better isolate causal relationships. The cluster pdfs that emerge in this idealized setting have reduced values of x_L, but possess the same τ value. The perturbations for all parameters except q_c are performed by multiplying the standard parameter value by a set of factors: [0.25, 0.5, 1.5, 2.0, 2.5]. The vapor threshold for strong precipitation q_c is perturbed by adding a set of factors, [210, 25, 5, 10, 15] in millimeters of CWV to its standard value (60 mm). Figure 3 presents the 1 mm h^{-1} threshold cluster pdfs for the different perturbed runs, and additional 0.5 mm h^{-1} threshold cluster pdfs for the α_c^{-1} perturbation runs. In Fig. 3, τ is fairly robust to the introduced perturbations, while x_L displays dramatic shifts, in the same vein as those documented in QN17a,b. There are also clear differences between the magnitudes of the a_L and c_L shifts, depending on the parameter being perturbed. Changes to σ, E, and q_c produce substantial shifts in both a_L and c_L. Changes to D_q and α_c^{-1}, however, appear to affect a_L more than c_L. The 1 mm h^{-1} cluster power pdfs, in particular, are insensitive to the admitted range of perturbations in α_c^{-1}; relaxing the precipitation threshold to 0.5 mm h^{-1} increases the c_L sensitivity to α_c^{-1}. Our goal with the parameter perturbation experiments was to identify the parametric controls on x_L. Interestingly, all the model parameters we tested for exert an influence on x_L, and therefore the scale of the precipitation clusters. Aside from the grid scale, the only imposed length scale in the idealized version of the model comes from the diffusion parameter D_q. The fact that the scales a_L and c_L are not associated *solely* with D_q—but have multiple controls—suggests that these scales are emergent properties that cannot be trivially tied to any single parameter. The physics of what controls x_L must therefore be probed in other ways (section 9).

Despite the multiple parametric controls on x_L, we wish to quantify the relative influence of each perturbed parameter on x_L. To do so, we must, first, however, measure x_L. A direct measurement of x_L from the pdfs involves curve-fitting procedures that can introduce additional sensitivities. We therefore, instead, leverage a property that associates x_L with the moment ratio x_M. The moment ratio of a distribution is defined as the ratio of its second moment to its first moment:

$$x_M = \frac{\langle x^2 \rangle}{\langle x \rangle},$$

where the operator $\langle \cdots \rangle$ measures the expected value of x from its distribution. For the particular functional form

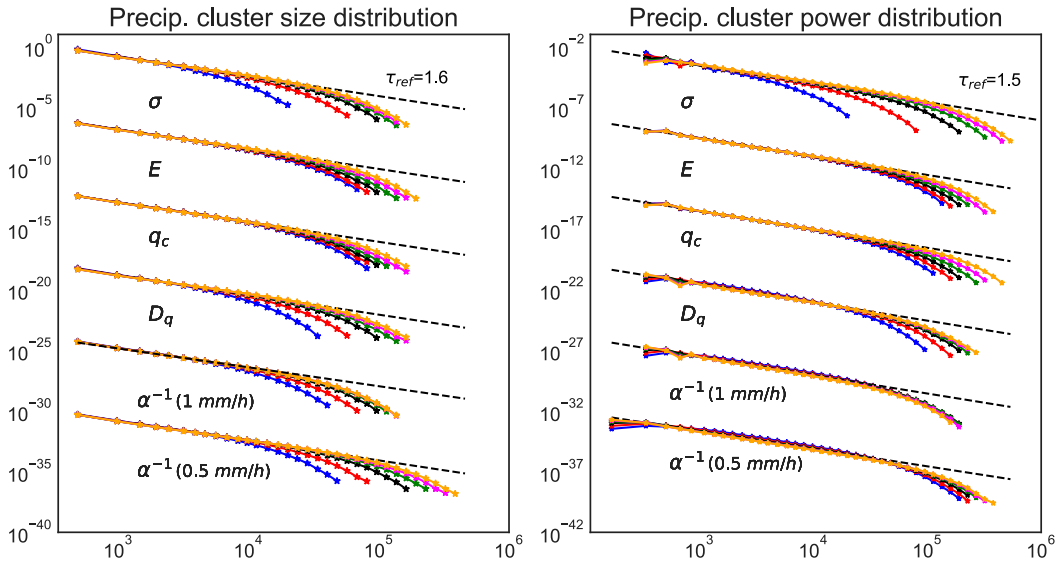

FIG. 3. The cluster pdfs for (left) size and (right) power that result from perturbations to five different model parameters: stochastic forcing amplitude σ, evaporation E, CWV threshold for precipitation q_c, diffusion coefficient D_q, and the moisture adjustment time α^{-1}. The parameters σ, E, D_q, and α^{-1} are perturbed with multipliers of 0.25 (blue), 0.5 (red), 1.5 (green), 2 (magenta), and 2.5 (orange), and q_c is perturbed with additive factors of −10 (blue), −5 (red), 5 (green), 10 (magenta), and 15 mm (orange). The black curve in each case indicates the cluster pdf with the standard parameter value from Table 1. Note that all the pdfs are for clusters constructed from a 1 mm h^{-1} threshold, except for α^{-1}, which has an additional set of pdfs for 0.5 mm h^{-1} threshold clusters. The slope of the cluster pdfs for the reference case (black) is indicated by τ_{ref}.

of the distribution given by (1), with τ fixed, we have the relationship (Peters et al. 2010; Neelin et al. 2017; Martinez-Villalobos and Neelin 2018):

$$x_L \propto x_M. \tag{12}$$

The value of τ is fairly robust to parameter perturbations (Fig. 3), a fact that then allows us to interpret changes in the easily computable x_M as corresponding linear changes in x_L, using (12). Figure 4 presents the percentage changes in x_M for both cluster size (Fig. 4a) and power (Fig. 4b), for the imposed parameter perturbations. The parameter perturbations are normalized by the reference value for each parameter allowing their presentation on the same scale. Note that we use a_M and c_M to indicate the moment ratios of cluster area and cluster power, respectively.

For the same perturbation factor, changes in q_c produce the largest shifts in x_M (both a_M and c_M), followed by changes in σ. For both these parameters, c_M shifts by a greater magnitude than a_M. For instance, an increase in q_c by 15 mm increases a_M by ~75%, but increases c_M by ~150%. Physically, this sensitivity to q_c perturbations can be understood as changes to the moisture convergence within the precipitating regime. For q_c increases that are not accompanied by compensating M_s increases,

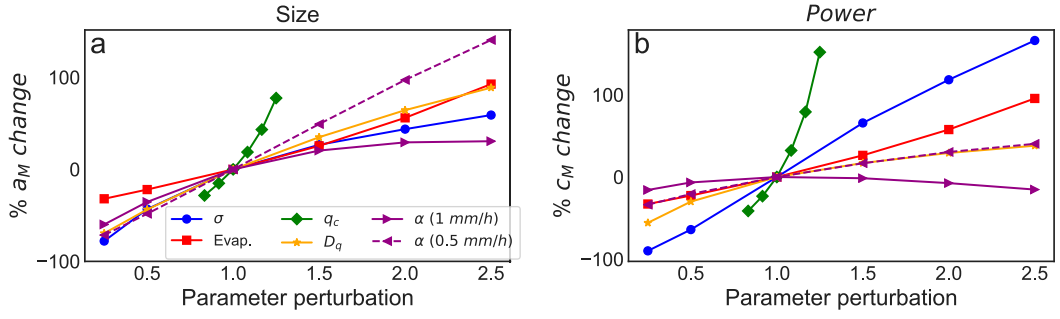

FIG. 4. The percentage change in (a) a_M and (b) c_M as a function of the perturbed variables on the x axis, each of which is normalized by its standard value (detailed in Table 1). Note the slightly different scales on the y axis for each panel.

the moisture convergence—the $(\nabla \cdot \mathbf{v}_1)q_v$ term in (4)—within the precipitating region also increases, leading to upward shifts in the precipitation cluster area and power cutoff. These numbers have implications for how the cluster distributions might change in a future climate, since q_c is projected to increase with global warming (Sahany et al. 2014). For instance, the closest analog in our parameter perturbation experiments to a 2-K warming is the q_c change from 60 to 70 mm, which produces increases in a_M and c_M by ~45% and ~80%, respectively.

Increasing σ by 2.5 times increases a_M by only ~50%, but increases c_M by ~150%. The shifts of x_M with increasing evaporation E are less dramatic (doubling E increases x_M by ~1.5 times). Changing the diffusion coefficient D_q produces about the same quantitative changes to a_M as E, but induces smaller c_M changes (doubling D_q only produces ~30% increase). The response to α^{-1} changes, as noted above, depends on the precipitation threshold used to construct the clusters. The use of 1 mm h^{-1} threshold produces subdued shifts in both the size and power; with c_M even showing a slight decrease at large parameter increases (~−15% change for 2.5 times reference α^{-1}). Reducing the threshold to 0.5 mm h^{-1} increases the x_M sensitivity to α^{-1}, but cluster size (~100% change in a_M for doubled α^{-1}) remains more sensitive than cluster power (~30% change in c_M for doubled α^{-1}).

Overall, increments in q_c and σ increase the frequency of large, powerful rain clusters. Increments in α^{-1} and D_q tend to increase the frequency of larger clusters without them necessarily containing more rain—pointing to the appearance of wider areas with weaker precipitation. Increases in E produces commensurate increments in the frequency of large precipitating systems with both increased size and power.

6. Process sensitivity

a. Experiment design

In this section, we examine the impacts of different physical mechanisms on the cluster distributions. To this end, we perform four primary mechanism denial experiments as described below. We will also discern the influence of rotational advection and the mock Hadley circulation on the cluster statistics.

(i) Specified Divergence: The use of the WTG divergence equation, (3), in the water vapor equation, (4), couples the divergence to precipitation. It is fairly well known that feedbacks between moisture convergence and latent heating can lead to mutual intensification. For increasing CWV, the moisture convergence increases if there is inadequate increase in the static stability M_s. This effect can also be viewed as decreasing gross moist stability (Neelin and Held 1987; Raymond et al. 2009; Inoue and Back 2015) with increasing moisture. The moisture convergence–latent heat coupling can therefore intensify precipitating regions and prolong their lifetimes. The additional constraint of a domain-mean nondivergence forces a compensating drying over nonprecipitating regions to match the precipitation enhancement over moist regions. Moisture convergence–latent heating coupling, therefore acts to impose a "rich get richer" aka "wet gets wetter, dry gets drier" situation (Chou and Neelin 2004; Held and Soden 2006; Chou et al. 2009), which in turn can favor convective aggregation. This coupling is switched off in the model by enforcing the following definition of divergence, $\nabla \cdot \mathbf{v}_1$:

$$\nabla \cdot \mathbf{v}_1 = -\frac{\xi}{M_s} \tag{13}$$

in the moisture and condensate equations, (4) and (5), halting interactions between the latent heating and the divergence field. Note that the divergence as specified in (13) is now purely stochastic.

(ii) Diffusion Only: Diffusion was a critical physical pathway in the HS15 model to generating precipitating clusters. Although diffusion can enhance nearest neighbor effects, we are wary of the trivial possibility that purely diffusive clusters dominate our statistics. We test for this possibility by operating the model under conditions where diffusion is the only relevant physical process. We make the divergence noninteracting and purely stochastic by substituting (13) in (4) and (5). We also remove the temporal autocorrelation by replacing (6) with $\xi dt = \sigma dW(t)$, where $dt = \Delta t$ in the numerical implementation. Our resulting stochastic divergence field is purely white (uncorrelated) in both time and space, similar to the noise field used in the HS15 model.

(iii) Diffusion Off: In our simple model, diffusion provides some nearest-neighbor connections in space by flattening local maxima and minima in the CWV and condensate fields. Although, we chose a standard value for our diffusion coefficient, D_q, such that the diffusive spindown time of a large precipitation cluster (~10^5 km^2) is ~$O(10)$ days, we do anticipate a role for small-scale mixing in precipitation clustering. We will test the importance of diffusion by setting $D_q = 0$ in both (4) and (5). Also note that smaller diffusive effects due to the numerical scheme exist even in the absence of explicit diffusion. We use this experiment without

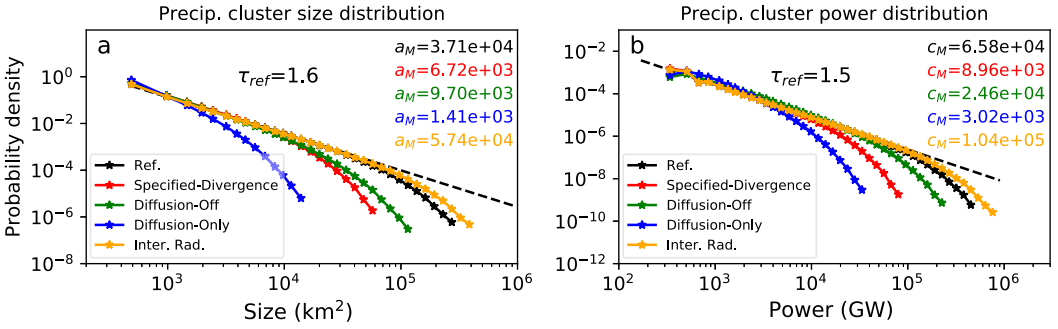

FIG. 5. The pdfs of precipitation (a) cluster size and (b) cluster power from different mechanism-denial runs described in section 6, indicated by different colors. The value τ_{ref} is power-law slope of the reference case (Ref.; black) fit over the power-law range using linear regression. The moment ratios a_M and c_M have the same units as the x-axis variable in each panel.

explicit diffusion to illuminate the importance of rotational advection. In fact, in a realistic regime, we expect the rotational wind to provide substantial "stirring" that can enhance the moisture gradients over which the small-scale diffusion operates (Eckart 1948; Villermaux 2019). We further elaborate on this property of rotational advection in section 6c.

(iv) Interactive radiation: In the standard model runs, we only considered the influence of spatially varying precipitation fluxes and neglect variations in the column radiative fluxes. It is well-documented that in cloud-permitting RCE domains, column radiative effects, through positive feedbacks with the circulation, marshal and maintain convection in an aggregated state (Bretherton et al. 2005; Muller and Held 2012; Emanuel et al. 2014; Wing et al. 2018). To test the role of interactive radiation in our model convective organization, we introduce a simple linear parameterization of F_{qre} and F_{cre} from (10):

$$F_{\text{qre}} = \varepsilon_r q_v, \tag{14}$$

$$F_{\text{cre}} = \varepsilon_{\text{cloud}}(P + P_{\text{cond}}). \tag{15}$$

Here ε_r (2.0 W m^{-2} mm^{-1}) and $\varepsilon_{\text{cloud}}$ (10.0 W m^{-2} mm^{-1} h^{-1}) capture the radiative effects of clear-sky CWV and the cloudy-sky effects of precipitation, respectively. The value of ε_r is estimated from typical values of F_s difference between moist and dry regions ($\sim$60 W m^{-2}, see Fig. 4a in Chou and Neelin 2003), divided by the typical difference in their CWV values ($\sim$30 mm, see Fig. 8 in Neelin et al. 2009). The estimate of $\varepsilon_{\text{cloud}}$ is less well constrained, but we take it as the typical cloudy and clear sky difference in column radiative flux convergence [$\sim$100 W m^{-2} for near saturation, see Fig. 10 in Wing and Emanuel (2014)], normalized by the precipitation in near-saturated columns [$\sim$10 mm h^{-1}, see Fig. 2a in Bao and Sherwood (2019)]. Note that (14) neglects to account for the subtleties of the vertical structure in moisture perturbations (Emanuel et al. 2014; Beucler and Cronin 2016), but captures the relevant leading-order effects of moisture–radiative interactions. According to (14) and (15), regions with higher CWV and precipitation will have larger values of F_s, leading to larger upper-level divergence via (3). Equations (14) and (15) are also used in section 9 to demonstrate how radiatively driven, self-aggregating precipitation clusters can emerge in certain parameter regimes.

b. *Results from mechanism-denial experiments*

Figure 5 compares the precipitation cluster statistics that emerge from the four different experiments, described above, in the presence of the both rotational advection and the mock Hadley cell. The precipitation clusters are created using the 1 mm h^{-1} threshold. The reference case (Ref., black curves) is the run with the standard parameter values detailed in Table 1. Shifts in the moment ratio x_M, and therefore the cutoff x_L toward higher values—with invariant τ—are interpreted as increases in the degree of organization and clustering. In Figs. 5a and 5b, the Specified Divergence run (red curves) sees reductions in a_L and c_L by factors of $\sim$5 and $\sim$7, respectively. The Diffusion Off run (green curves), by comparison sees reductions in a_L and c_L by factors of $\sim$4 and $\sim$2.5, respectively. The Diffusion Only run (blue curves) has by far the largest reductions in x_L: by factors of $\sim$26 and $\sim$21 for a_L and c_L, respectively. In fact, the cluster power and size distributions for the Diffusion Only run no longer possess a distinct power-law range. The results here imply that moisture convergence–latent heating feedbacks are the primary physical process supporting the aggregation of convection in the standard model configuration. Diffusive mixing aids the creation of large precipitating clusters, but does not generate adequate clustering by itself. The Interactive Radiation run (orange curves) in Figs. 5a and 5b shows increases

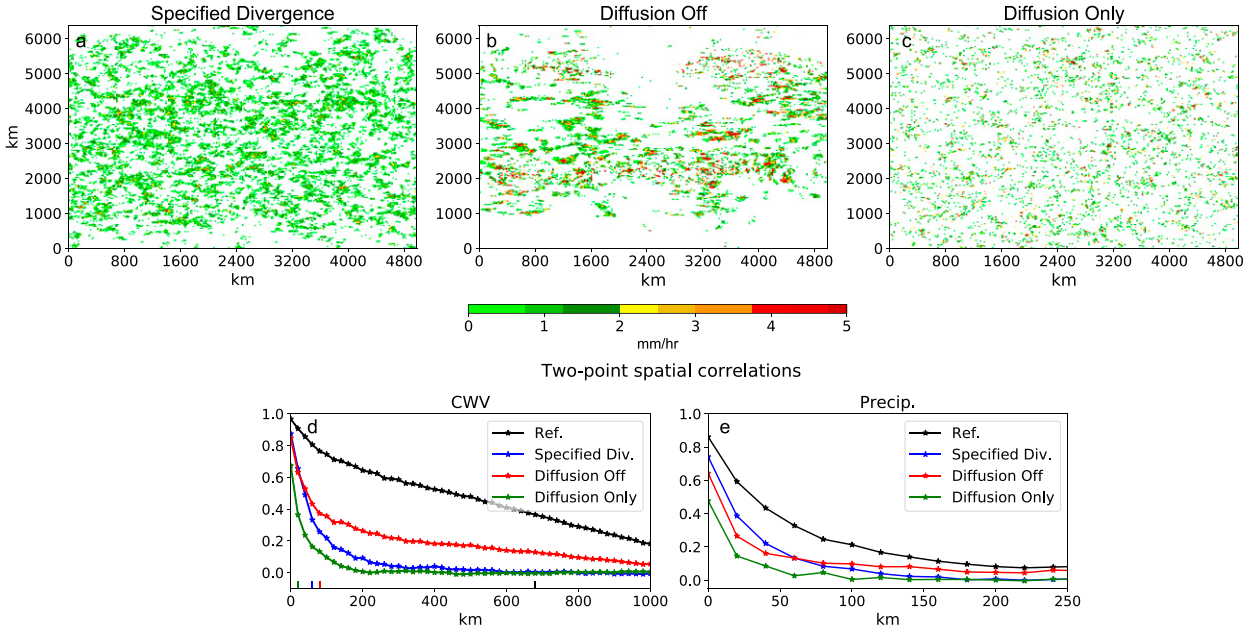

FIG. 6. The precipitation fields for (a) Specified Divergence, (b) Diffusion Off, and (c) Diffusion Only runs on day 73, hour 6, as in Fig. 1. The two-point spatial correlations for the (d) column water vapor (CWV) and (e) precipitation (Precip.) for four different runs—including the reference run (black)—are shown in (d) and (e). The colored dashes on the x axis in (d) mark the e-folding distances for the CWV field for each run. Note that (d) and (e) have different x-axis scales.

in x_L (by a factor of ~1.5). Interactive radiation, as parameterized in (14) and (15), is designed to amplify the moisture convergence–latent heating feedbacks, and is therefore capable of extending the scale of large precipitation clusters. Interactive radiation is, however, not the leading cause of precipitation clustering in this model.

Figure 6 presents a set of additional diagnostics from the runs discussed in Fig. 5, excluding the Interactive Radiation run (which is only marginally different from the Ref. case). Figures 6a–c can be directly compared to Fig. 1. Figure 6a shows how the exclusion of moisture convergence–latent heating interactions removes the influence of the mock Hadley cell. The regions near the northern and southern boundaries are now inhabited by precipitation clusters, in contrast to Fig. 1. Visually, the precipitation clusters in Fig. 6a are less clearly separated by nonprecipitating regions than in Fig. 1. Figure 6b is a snapshot from the Diffusion Off run that shows precipitation clusters more organized than those in Fig. 6a. The precipitation rates in some regions, however, are exceedingly high (in excess of 10 mm h^{-1}). Without explicit diffusion to flatten the CWV gradients, the moisture convergence–latent heating feedbacks introduce a tendency to produce "gridpoint storms" for the parameter set used in the Diffusion Off run. These highly concentrated areas of precipitation explain the slightly smaller reductions in c_L (~2.5) compared to a_L (~4), noted in the previous paragraph. The precipitation field from the Diffusion Only run (Fig. 6c) visually confirms the lack of large precipitation clusters, as inferred from the cluster size and power distributions in Figs. 5a and 5b. Figures 6d and 6e present the two-point spatial correlation curves for the CWV and the precipitation field, respectively: another way of visualizing the differences in x_L between the different runs. The CWV and precipitation fields both show the largest spatial correlations (indicated by the e-folding distance in Fig. 6d) for the Ref. run. The absence of both diffusion and moisture convergence–latent heating coupling have substantial impacts on the CWV spatial correlation structure. Comparing the two-point precipitation spatial correlation structure between Specified Divergence and Diffusion Off in Fig. 6d highlights an interesting behavior. The spatial correlations are comparable for the first 50 km, but the tail of the Diffusion Off curve (in red) decays more slowly at larger distances up to 250 km, compared to the Specified Divergence curve (in blue). This suggests that moisture convergence–latent heating feedbacks, in conjunction with the large-scale features, induce long-range correlations in the spatial correlation structure of precipitation.

c. *Roles for rotational advection and the mock Hadley cell*

All the runs discussed in section 5 included the influence of the mock Hadley cell and the rotational

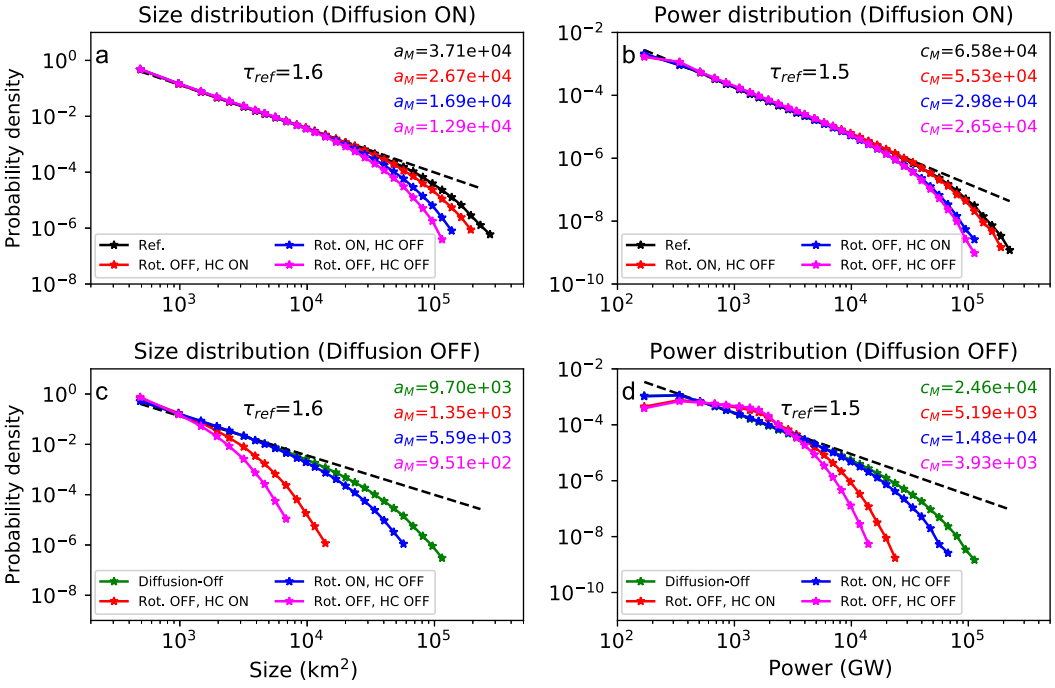

FIG. 7. As in Fig. 5, but for model experiments aimed at testing the relative influence of diffusion, the mock Hadley cell, and rotational advection on a_M and c_M. Diffusion is (a),(b) present and (c),(d) absent. In all panels, the blue curves indicate runs with rotational advection and without the mock Hadley cell (ROT ON, HC OFF), the red curves indicate runs without rotational wind advection and with the mock Hadley cell (ROT OFF, HC ON), and the magenta curves indicate runs without both the rotational wind advection and the mock Hadley cell (ROT OFF, HC OFF). The black reference curves in (a) and (b) are repeated from Fig. 5, the green reference curves in (c) and (d) are from the Diffusion Off run in Fig. 5. The value τ_{ref} is the power-law slope of the reference case.

advection. We now examine the individual impacts of these processes on precipitation clustering. Figure 7 shows the impacts of turning off one or both of these features—with (Figs. 7a,b) and without diffusion (Figs. 7c,d). The Ref. case in Figs. 7a and 7b (black curves) is repeated from Figs. 5a and 5b. When both the rotational wind advection and the mock Hadley cell are turned off (blue curves), there is a reduction in a_M (3.71×10^4 versus 1.29×10^4 km^2) and c_M (6.58×10^4 versus 2.65×10^4 GW). This clarifies that the combination of both the rotational advection and the mock Hadley cell act to increase x_L. Comparing the black and green curves in Figs. 7a and 7b show that the influence of rotational advection—in the presence of explicit diffusion—is only marginal (reductions in a_L and c_L by factors of ~1.4 and ~1.2, respectively). Comparing the black and red curves shows that the mock Hadley cell is slightly more impactful (reductions in x_L by a factor ~2.2).

Figures 7c and 7d compare the relative impacts of the mock Hadley cell and rotational advection in the absence of explicit diffusion. The green curve in these figures is repeated from the Diffusion Off experiment of Figs. 5a and 5b. In the absence of diffusion, the removal of rotational advection results in a substantial decreases in both a_L and c_L (by factors of ~7.2 and ~4.7, respectively). Moreover, the power-law portions of the cluster pdfs vanish (red curves in Figs. 7c and 7d), implying that organized precipitation features are absent in these runs, a fact that we also confirmed visually (not shown). In contrast, the removal of the mock Hadley cell is less drastic—resulting in x_L reductions of ~1.7, comparable to its effects in the presence of diffusion (~2.2). These results suggest that rotational advection—as anticipated—assumes significance in the physics of precipitation clustering when *explicit diffusion is absent*. These results underscore the role of a lateral mixing—or more generally, a neighbor communication process—in generating precipitation clusters. Precipitation intensification, acting on its own, without any form of lateral mixing is unable to generate organized precipitation clusters. Substantial diffusion effectively executes this mixing (Fig. 5). When explicit diffusion is absent, rotational wind advection aids lateral mixing (Fig. 7), playing a role similar to the process of stirring-enhanced mixing (Eckart 1948; Welander 1955), wherein the CWV field is elongated in space to enhance the gradients over which the small-scale numerical diffusion

operates. The rotational advection can therefore be thought of as increasing the effective diffusivity of the model (Lin et al. 2010).

The precipitation clustering in this model is governed by two sets of physical processes: the first set acts to increase the intensity and persistence of convection, and the second set encourages precipitation in the neighborhood of existing precipitation. The former set encompasses moisture convergence–latent heating feedbacks, temporal persistence in the random divergence source, and moisture– and cloud–radiative feedbacks. The latter set includes diffusive mixing, whose efficacy can be enhanced by rotational advection.

7. Relationship to percolation models

Percolation models (Stauffer and Aharony 1992) are useful null models for meteorological clusters—as explored in Peters et al. (2009). The simplest example of this class of models is site percolation, for which sites on a lattice are randomly filled or emptied with a given probability p_0, and the clusters that result from the connected sites are evaluated. A domain with a distribution of connected clusters is said to be percolating if there exists at least one cluster that spans the length of the domain in any direction. The properties of the cluster distribution are well-known for infinite-sized lattices, around the p_0 value for which the percolating cluster first appears. At this critical value, the probability distribution of the cluster sizes is a pure power law, that is, the cutoff $a_L \to \infty$. The slope of this power law for an infinite-sized, two-dimensional square lattice is $\tau \sim 2.05$. It is worth noting this slope can vary depending on the distance to percolation: as a lattice model moves from a nonpercolating state toward percolation, its slope tends to increase to $\tau \sim 2.05$ (Ding et al. 2014). It might be tempting to interpret the observed precipitation cluster distribution slopes as a function of the distance to percolation; but Ding et al. (2014) did not note a stable regime around $\tau \sim 1.5$.

Percolation clusters also lack an inherent spatial scale and rely on the grid size for scale. In such models, x_L would change with the grid size: an undesirable property for quantities such as the horizontal scale of tropical convective systems including MCSs and superclusters. To test for this degenerate result we simply reran the reference case (Ref.) with a halved grid size, that is, $\Delta x' = \Delta x/2$ and $\Delta y' = \Delta y/2$. The halved-grid-size case has twice the σ value from the reference case, in accordance with central limit theorem. The Gaussian noise amplitude in the larger grid should be smaller by a factor of $\sqrt{4}$ when compared to σ in each of the four subgrids. The results comparing the Ref. case with the halved grid-size case are shown in Figs. 8a and 8b. Note that the Ref. case is shifted vertically to overlie with the halved grid case to establish the sameness of their slopes; this is equivalent to a change in the normalization constant, which differs due to the different minimum size or power associated with the change in resolution. Figures 8a and 8b show that the slopes τ and the moment ratios x_M for the two cases vary by less than 10%. This lack of change when compared to the factor-of-4 change in the grid size shows that the cluster statistics are independent of the grid size. This suggests that x_L in our model is a property of the physics and not the numerical grid. Figures 8c and 8d show runs from two different site percolation runs (with $p_0 = 0.4$ and $p_0 = 0.55$, respectively). These cases have τ values that bracket the observed value ($\tau \approx 1.4$ and 1.7), but with drastic differences in the cutoff. Note that both τ and x_L in percolation models are controlled by the single parameter p_0 (Ding et al. 2014), such that τ steepens as p_0 approaches the critical p_0. Further increases in p_0 toward the critical value ($\approx$0.59), yield τ values that approach the percolation slope at criticality, $\sim$2 (not shown). The clusters in the percolation model are also sensitive to the grid size; decreasing the grid size by a factor of 4 produces a corresponding change in x_M by the same factor. In other words there is no physical scale corresponding to the cutoff in the percolation model. The lack of a robust τ value and sensitivity to grid size therefore rule out the percolation model as a satisfactory prototype for precipitation clusters.

There are, however, aspects for which information from percolation models can be qualitatively relevant. Finite-sized domains can percolate even in the physically based model. In other words, a domain-spanning cluster can appear if the domain area a_d is small enough ($a_d \lesssim a_L$). In such situations, the relative frequency of smaller clusters increases at the expense of larger clusters, and leads to increases in τ. In the online supplement (Fig. S7), we show how this effect can come into play even in our model. It is plausible that these finite-sized effects played a part in the large τ values ($\sim$2) reported in Peters et al. (2009), who sampled precipitation clusters in highly moist environments within narrow satellite swaths. The percolation model also serves as a foil to illustrate an important property of the physical model. Whereas in the percolation model, the cutoff simply shifts as grid size changes, in the physical model the cutoff is independent of grid size. In other words, in the physically based model, the cutoff is indeed a physical scale.

8. The stochastic branching process as an analog for convective organization

In this section, we seek an alternative prototype to percolation models that is both simple and yet contains

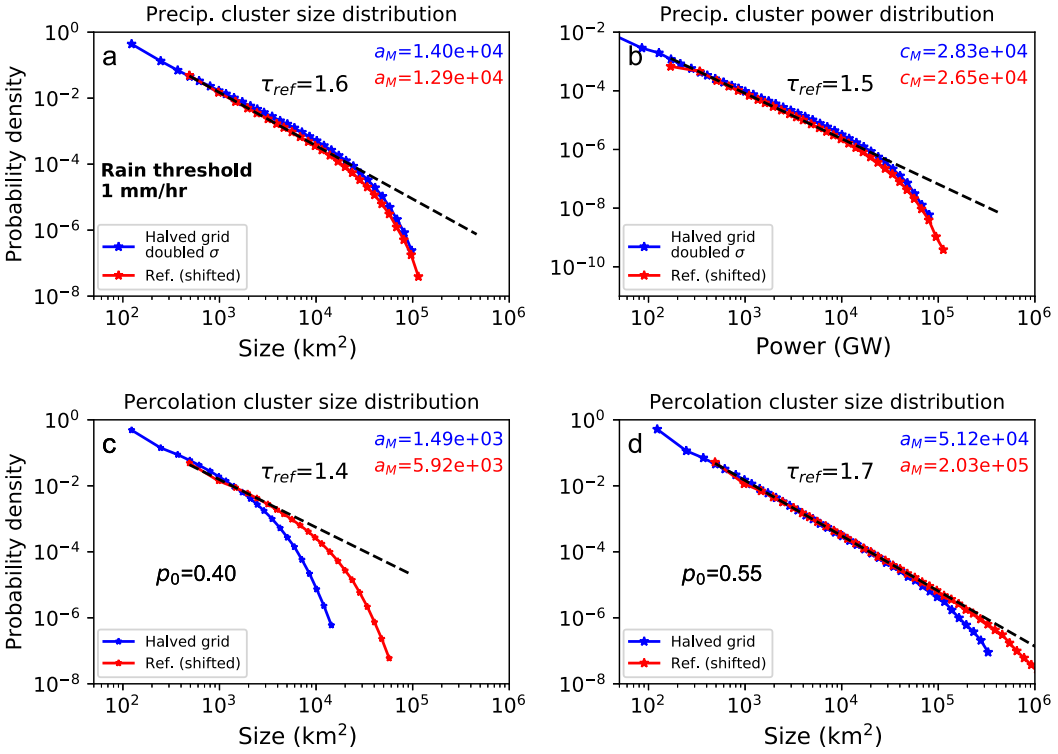

FIG. 8. (a),(b) As in Fig. 5, but comparing the reference case (red) with a case where the grid size in the model is halved (blue). (c),(d) Comparison of the cluster size pdfs from two site percolation runs, with probabilities of occupation $p_0 = 0.4$ and 0.55, respectively, and both with the original grid size (red) and halved grid size (blue). The reference line is shifted vertically so that the power-law portions of both the pdfs nearly overlie each other. Note that this shift corresponds to a change in the normalization constant of the reference-case pdf.

features analogous to the physics of convective organization. One appealing candidate is the stochastic branching process (SBP) or the Galton–Watson process (Harris 1963; Kendall 1966; Athreya and Ney 2011). This process was first conceived of in work that modeled the likelihood of family tree extinctions (Watson and Galton 1875).

a. Background

The principle behind the SBP is straightforward. Assume that there exists a single "seed" at an initial time t_0. After the passage of an arbitrary time interval, the seed branches out and gives rise to one or more "descendants." Each of these descendants in turn spawns its own progeny, creating a sizeable family tree after a few generations. Under these conditions, analytical forms are available for the asymptotic size of the tree, that is, a size large enough such that the number of new additions is much smaller than the total size. The parameters of this size distribution are dependent on the distribution governing the number of branches spawned out of any given seed. If we assume that this "branching probability" follows a Poisson distribution, then we obtain the following distribution $p'(s)$ for the total size of the tree:

$$p'(s) \sim s^{-3/2} \exp\left(-\frac{s}{s_L}\right), \tag{16}$$

where s is the size of the tree. If λ is the mean number of branches per generation that characterizes our Poisson distribution, then the cutoff s_L is given by

$$s_L = \frac{1}{\lambda - 1 - \ln\lambda}. \tag{17}$$

Note that (16) is in the same form as (1). The derivation of (16) relies on the assumption that the branching probability is independent of the tree size or generation. This derivation appears to be well known in the SBP literature, but a brief sketch is provided in the supplement for reference. Equation (16) is also not dependent on the assumption of Poisson distribution. Other treatments with different forms for the branching probability also arrive at the same value of τ [Vere-Jones 1977; Alstrøm 1988; also see Sornette (2006) for more examples]. The cutoff s_L in these cases, though still dependent

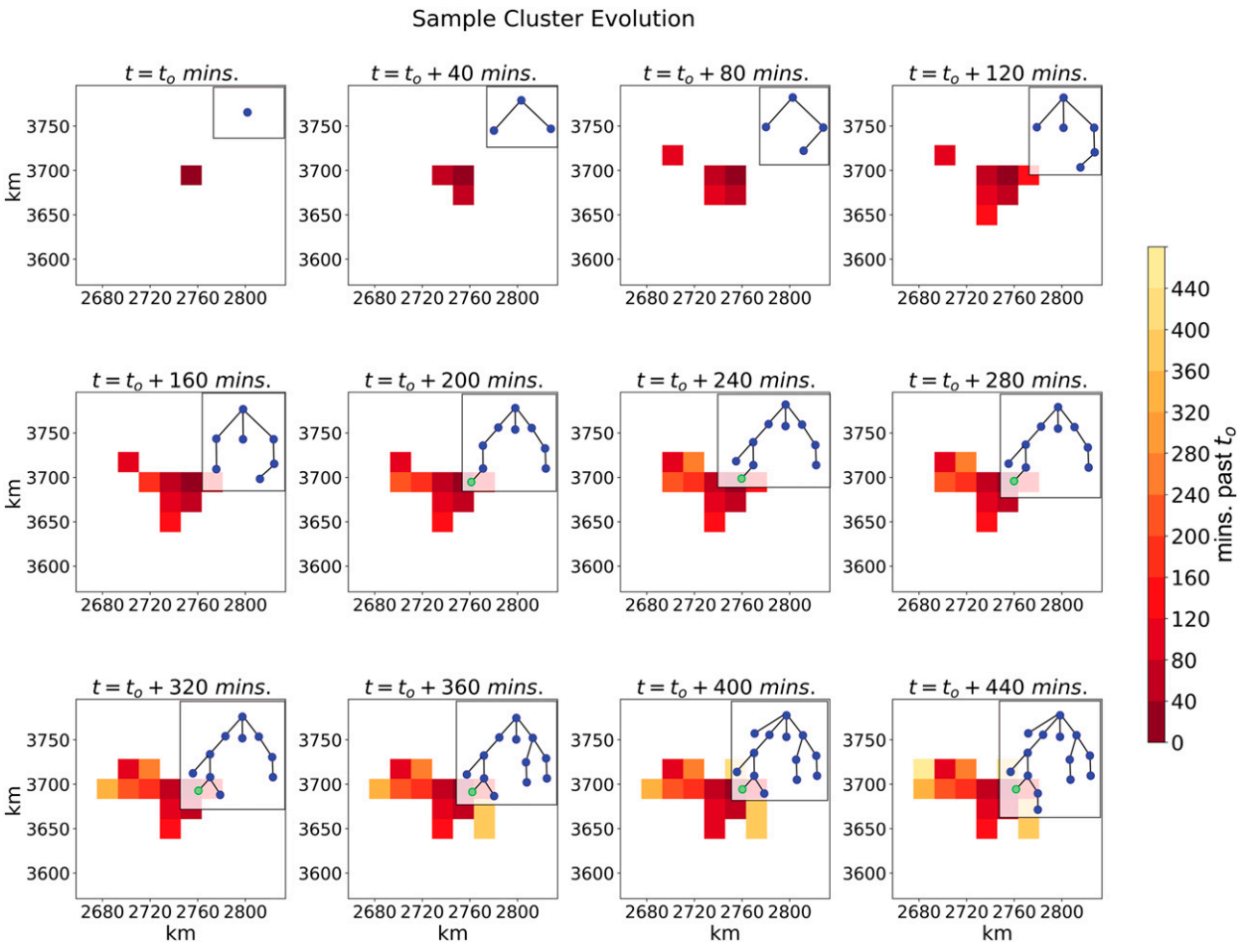

FIG. 9. A zoomed-in view of the evolution of a sample precipitation cluster over a time period of ~7 h, used to demonstrate analogies between precipitation cluster growth and a branching process. Time increases from left to right in each row. One possible mapping to the stochastic branching process is provided in the inset in each panel. The blue nodes of the branch represent precipitating pixels that are part of the tree; the green nodes represent pixels that merge with the tree. The precipitating pixels are colored by their time of appearance, with darker pixels arriving earlier. Note that this mapping only tracks cluster growth and does not account for precipitating pixels, which may decay during cluster expansion.

on the branching probability, differs from (17) in its functional form. We will, however, for demonstration purposes, assume a Poisson distribution for our branching probability. It is also worth noting that the condition of asymptotic convergence implies that $\lambda < 1$, that is, there is a zero probability of a tree growing indefinitely. The condition $\lambda \geq 1$ would imply a tree that has a finite probability of growing indefinitely.

b. *Mapping to cluster size and power distributions*

We now elaborate the analogies between the SBP and cluster growth. Precipitation clusters can be thought to primarily grow by spawning precipitating regions adjacent to existing precipitation [e.g., as documented in López (1978) and Cheng et al. (2018)]. The actual process that facilitates this growth is immaterial and can assume many forms, including density currents (Tompkins 2001; Feng et al. 2015; Torri et al. 2015), gravity waves (Mapes 1993; Fovell 2002), lateral spreading of stratiform precipitation from a convective core (Houze 1997), or lateral mixing by diffusion (HS15), aided by the rotational wind (this study).

Each precipitating pixel that develops adjacent to an existing precipitating pixel is thought of as a "branch" in the SBP. Precipitation clusters are then analogous to trees from the SBP, where the pixels in the interior are the antecedents and the pixels on the cluster perimeter are the newest members of the tree. This analogy is graphically presented in Fig. 9, following the evolution of a precipitation cluster from a single pixel, and the analogous evolution of the branching process in the inset on each panel. In Fig. 9, new precipitating regions

emerge from a precipitating pixel by ''branching'' outward. In this mapping, λ corresponds to the average number of precipitating pixels that emerge adjacent to an existing precipitating pixel, in a given time interval. If real precipitation clusters grow by some mechanism akin to the branching process, it would explain why the cluster size distribution follows a power-law distribution—with slope = −1.5—and also possess an exponential cutoff. The precipitating pixel is also likely to excite new *nonadjacent* precipitating points; these points can grow by their own adjacent branching process before merging with the parent cluster. Since the expressions in (16) and (17) are still valid for a small number of mergers between trees, the parameters of the cluster distribution will remain robust to mergers between clusters.

As the precipitation cluster grows in two horizontal dimensions, the branching is influenced by the number of surrounding precipitating points. This imposes limits on the number of branches that can spawn in each generation, violating the assumption of independent branching. This restrained cluster growth might explain the slight deviation of the observed cluster size distribution slope from −1.5 to a slightly steeper value of −1.66 (QN17a; Teo et al. 2017). A similar line of reasoning can be applied to map the trees from the SBP to cluster power increases. An arbitrary unit of precipitation is considered to be a single branch. The cluster power can branch out by spawning adjacent precipitation points—as in cluster size growth—but also by precipitating harder in existing points within the cluster. This branching can therefore proceed in a higher-dimensional ''precipitation space'' as opposed to the two-dimensional horizontal plane for cluster size. This added degree of freedom for cluster power branching might also explain why the observed value of τ is closer to 1.5 for cluster power distributions, than for cluster size distributions.

We note that there are limits to the SBP–precipitation cluster analogies with regard to cluster decay that are worth highlighting. The connections between the precipitation clusters and the SBP are only valid in the cluster growth phase. As the cluster–SBP relationship is quantified here, preexisting branches cannot undergo ''deaths'' during the spawning process, when the cluster is branching outward. This may not be a strong limiting factor *within growing clusters*, as these interior ''holes'' can be reinitiated by neighboring pixels—so preexisting branches can effectively persist longer than the time scale of branching. The SBP as presented here also does not address how the cluster size distribution would change as the precipitation clusters stop growing and begin to shrink. A similar stochastic ''culling'' process might apply for cluster decay. We will, however, defer these considerations to future efforts and proceed to test the utility of the cluster–SBP analogs for our model.

c. *Testing the applicability of the stochastic branching process*

One hitherto unexplained aspect of our cluster distribution is the sensitivity of the cutoffs x_L to perturbations in multiple model parameters (Figs. 3 and 4). If the SBP is relevant to precipitation clustering, then the expression in (17) should be able to capture aspects of this multiparameter dependence. To test for this possibility, we first devise a nearest-neighbor probability metric λ_{nn} intended to capture the average number of neighbors spawned by a precipitating element, in a chosen time interval. An accurate estimation of λ_{nn} would involve tracking the relationship between several precipitating pixels and the pixels that arise in their neighborhood across multiple generations: a fairly cumbersome and impractical exercise. We therefore choose a practical, aggregate measure that captures some aspects of λ from the SBP. In our mapping (Fig. 9), a precipitating pixel passes from current to previous generation when it first attains 4 nearest neighbors—as it can no longer spawn more neighbors. We suitably define λ_{nn} as

$$\lambda_{\mathrm{nn}} = \sum_{z=1}^{4} z p_b(z), \tag{18}$$

where $p_b(z)$ is the probability that a precipitating pixel spawns z neighbors. We use the following definitions to estimate p_b:

$$p_b(1) = \left.\frac{n_{3\mathrm{nn}\to 4\mathrm{nn}}}{N}\right|_{\Delta t=6\mathrm{h}},$$

$$p_b(2) = \left.\frac{n_{2\mathrm{nn}\to 4\mathrm{nn}}}{N}\right|_{\Delta t=6\mathrm{h}},$$

$$p_b(3) = \left.\frac{n_{1\mathrm{nn}\to 4\mathrm{nn}}}{N}\right|_{\Delta t=6\mathrm{h}},$$

$$p_b(4) = \left.\frac{n_{0\mathrm{nn}\to 4\mathrm{nn}}}{N}\right|_{\Delta t=6\mathrm{h}}.$$

Here, $n_{3\mathrm{nn}\to 4\mathrm{nn}}$ is number of precipitating pixels that transition from having 3 nearest neighbors to 4 nearest neighbors, within a time interval Δt. The denominator N denotes the total number of pixels that remained active (did not stop precipitating) during the considered time interval. We base our value of Δt on the most typical duration of observed convective systems (e.g., Machado et al. 1998), but we found no qualitative changes to our results upon varying the length of this time window between 4 and 12 h (not shown).

We can similarly approximate cluster power as branching in its own precipitation space. Cluster power

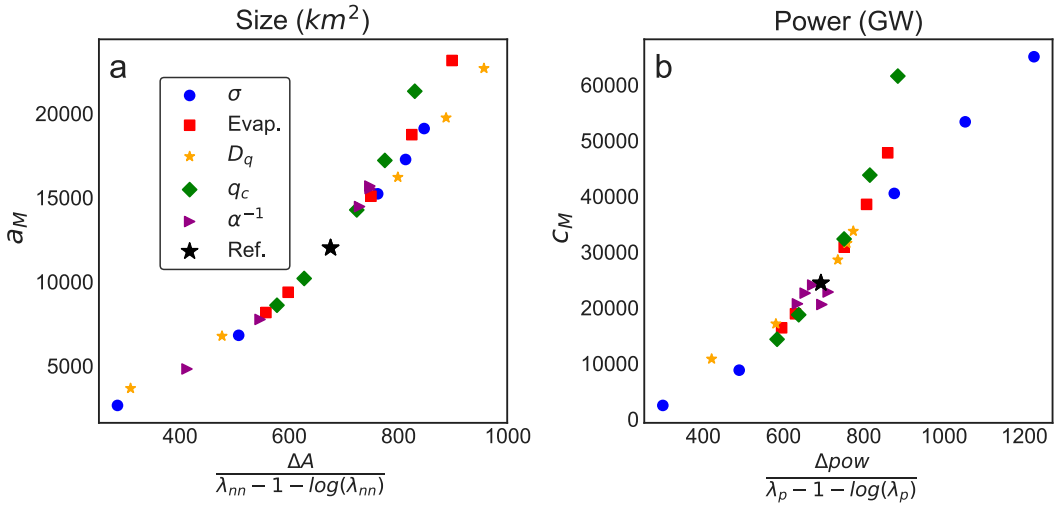

FIG. 10. (a) Changes in a_M from the parameter perturbation experiments (section 5), plotted as a function of the cutoff computed from (17) using λ_{nn} from (18). (b) A similar plot for c_M vs the cutoff computed using λ_p from (19). See text for more details on λ_{nn}, λ_p, and the branching process. The black star denotes the reference-case a_M and c_M in each panel, and the other markers denote the different parameters being perturbed. ΔA and Δpow are the area of a single pixel ($\approx$488 km^2) and the power contained within a single pixel precipitating at 2 mm h^{-1} ($\approx$678 GW), respectively.

is not discrete like cluster area on a grid, but for purposes of mapping to the SBP, we discretize the power using an arbitrary precipitation rate. We postulate this discretized power as a pragmatic measure and we will test its utility for analysis of the full model. Every new branch in the cluster area space is also a new branch in the cluster power space, we therefore use λ_{nn} as the basis for a similar nearest neighbor probability metric for cluster power λ_p:

$$\lambda_p = \frac{1}{\delta \mathrm{Pr}} \frac{\Delta \mathrm{Pr}_{3nn\to 4nn} + \Delta \mathrm{Pr}_{2nn\to 4nn} + \Delta \mathrm{Pr}_{1nn\to 4nn} + \Delta \mathrm{Pr}_{0nn\to 4nn}}{N}\bigg|_{\Delta t=6h}, \tag{19}$$

where $\Delta \mathrm{Pr}_{3nn\to 4nn}$ is the total precipitation increase during the 3nn$\to$4nn transition. Parameter δPr is an arbitrary amount of precipitation that was chosen to constitute one "precipitation branch" (δPr = 2.0 mm h^{-1}), such that $\lambda_p < 1$. λ_p simply tracks the average change in precipitation within the transitioning pixels, during a time interval of Δt, and discretizes this change with an arbitrary amount δPr to ensure that $\lambda_p < 1$.

We now use (18) and (19) to compute a neighbor probability for each of the perturbed runs from section 4. We take the mean of these neighbor probabilities across all the sampled 6-h intervals, and then use (17) to reconstruct the cutoff for the cluster size and power. This quantity is then multiplied by the size of one pixel and the power contained in a single pixel precipitating at δPr = 2 mm h^{-1}, to convert s_L for size and power to units of square kilometers and GW, respectively. The x_M values for the different parameter perturbations discussed in section 5 are plotted against the cutoffs computed using the neighbor probability metric in Fig. 10. At first glance, λ_{nn} and λ_p appear to capture the variations in x_M across all parameter perturbations. The collapse between a_M and λ_{nn} (Fig. 10a) is more striking than the collapse between c_M and λ_p (Fig. 10b). However, λ_p still captures features noted in section 5, such as the insensitivity of the 1 mm h^{-1} cluster power to variations in α^{-1}, and the larger changes in a_M when compared to c_M, following D_q perturbations. The sensitivity of x_L to multiple model parameters is therefore apparently reducible to a single parameter (λ_{nn} for size and λ_p for power).

9. Radiatively driven convective self-aggregation

Under RCE, the radiative effects of water vapor and clouds can drive the water vapor field to aggregate in cloud-permitting models (Bretherton et al. 2005; Muller and Held 2012; Jeevanjee and Romps 2013; Wing and Emanuel 2014; Muller and Bony 2015). Our model—also run under RCE—is capable of supporting self-aggregating clusters, albeit in a different parameter regime than the ones explored thus far. Note that for consistency with the wider literature in this area, we will

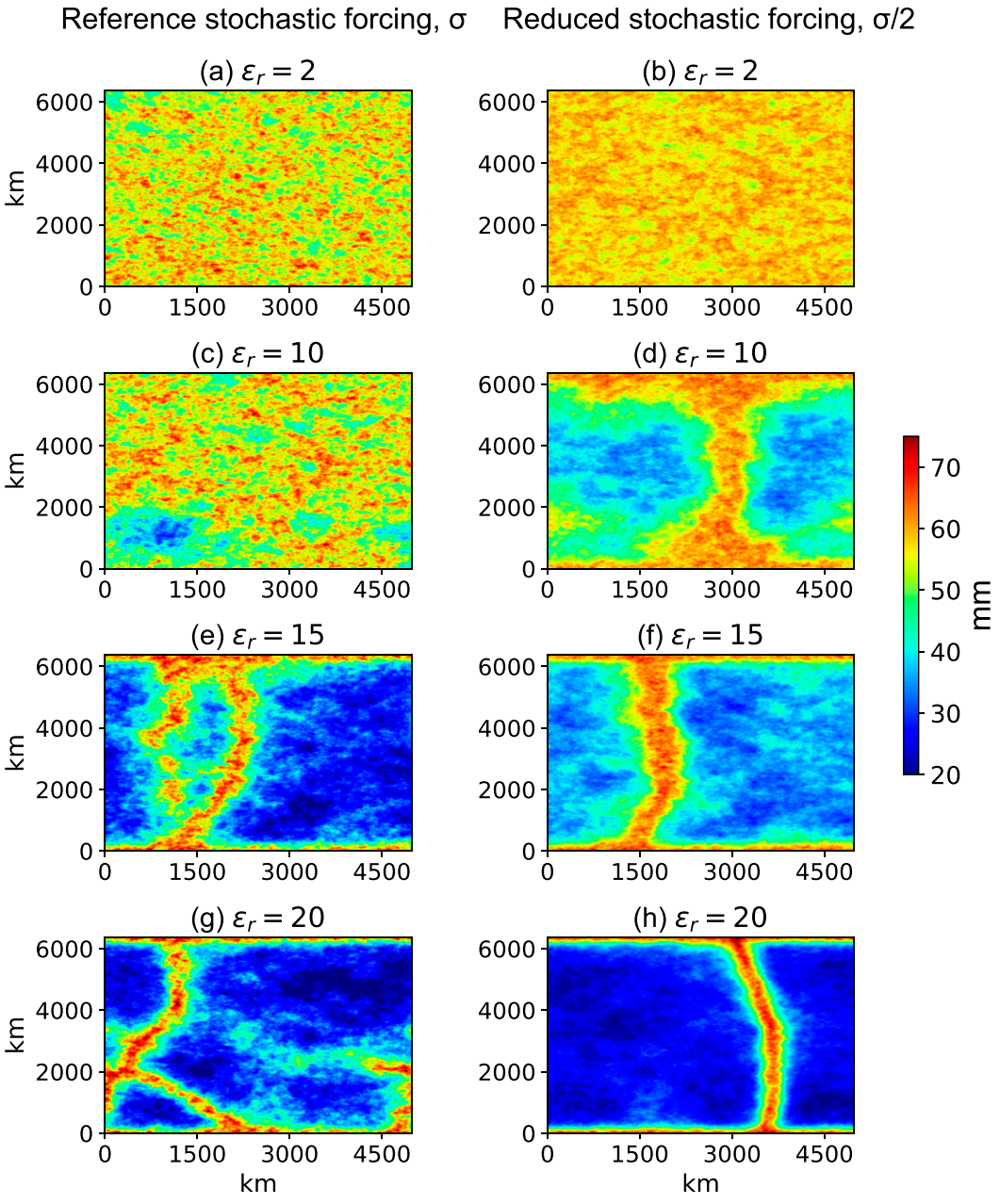

FIG. 11. CWV field at day 365 for sets of runs with perturbations to the moisture–radiative feedback parameter ε_r, with (left) reference stochastic forcing σ from Table 1 and (right) reduced stochastic forcing $\sigma/2$. Values of ε_r ($\mathrm{W\,m^{-2}\,mm^{-1}}$) for each run are shown in the panel titles.

use the terms "self-aggregation" and "self-aggregated clusters" to denote clustering driven primarily by radiative feedbacks. The clusters dominated by other feedbacks of the moist physics are also—strictly speaking—self-aggregating. We encourage the emergence of self-aggregating clusters by directly perturbing the strength of the moisture–radiative feedback ε_r in (14). We run the model without the mock Hadley cell to ensure spatially uniform conditions. We test the results of increasing ε_r by factors of 5, 7.5, and 10, for two sets of runs: with reference and reduced values of the stochastic forcing σ. Figure 11 shows the CWV field on day 365 of each run. The runs with the standard value of ε_R in Figs. 11a and 11b show a nearly homogeneous distribution of CWV, corresponding to a homogeneous precipitation cluster distribution, though the run with reduced σ (Fig. 11b) shows smaller spatial variability. Increasing ε_r by a factor of 5 ($10\,\mathrm{W\,m^{-2}\,mm^{-1}}$) induces the onset of

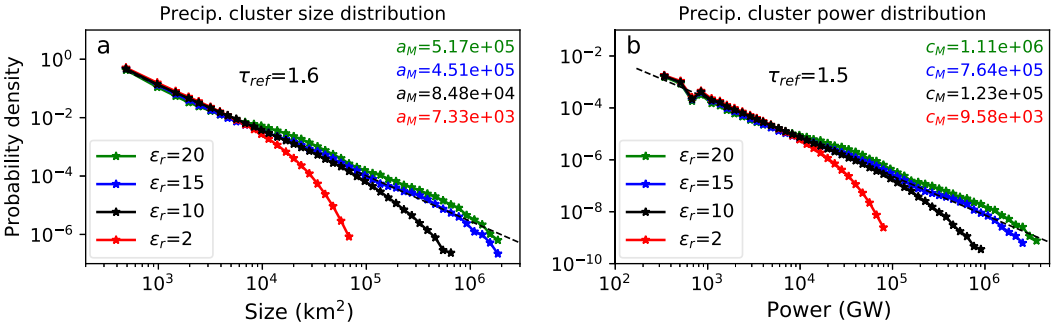

FIG. 12. As in Fig. 5, but for the runs with the weak stochastic forcing shown in Fig. 11. The black (ε_r = 10 W m^{-2} mm^{-1}), blue (ε_r = 15 W m^{-2} mm^{-1}), and green (ε_r = 20 W m^{-2} mm^{-1}) curves exhibit increasing degrees of self-aggregation.

self-aggregation in the run with small σ (Fig. 11d), that is, the dry and moist regions are spatially well separated. The run with reference σ value (Fig. 11c) responds with larger spatial variability but without a clear moist–dry separation, though a noticeable dry patch is visible in the southwest corner of the domain. Further increase in ε_r to 15 W m^{-2} mm^{-1} induces the onset of self-aggregation in the reference σ run (Fig. 11e), but with the aggregated state less coherent than its counterpart run with reduced σ (Fig. 11f)—which is visually reminiscent of clusters in RCE channel models (Wing and Cronin 2016). Even with ε_r set to 20 W m^{-2} mm^{-1}, the moist–dry separation in the reference σ case (Fig. 11g) is more diffuse than in the reduced σ case (Fig. 11h). The onset of the self-aggregation regime in our model is therefore contingent upon the relative strengths of the radiative feedbacks and the random variability. The qualitative picture in Fig. 11 is not affected by the presence of rotational advection, though the aggregated CWV field is more spatially elongated (not shown). Examples of more exotic variants of self-aggregation, driven purely by instabilities in the nonstochastic version of the model are shown in the online supplement (Fig. S9).

To assess the relevance of the self-aggregated regime to the cluster distributions in our model, we present the cluster pdfs in Fig. 12 for four of the runs with reduced σ, since the effects of self-aggregation are more apparent in this set. The cluster pdfs for the run with ε_r = 2 W m^{-2} mm^{-1} show a power-law range with a cutoff that is diminished, and consistent with the results of the parameter perturbation experiments in section 4. The cluster pdf with ε_r = 10 W m^{-2} mm^{-1}—that had commenced self-aggregation in Fig. 11d—shows the same value of τ as our other reference cases, but with a less clearly defined cutoff. The runs with the strongly self-aggregated CWV field (green curves) have pdfs with a noticeable peak ~2–5 × 10^4 km^2 and ~7–8 × 10^4 GW. The runs with ε_r = 15 W m^{-2} mm^{-1} (blue curves) even hint at two peaks in the cluster pdfs. These peaks indicate a preferred scale for clusters in these runs, and signal a departure from the canonical pdfs described by (1). Our model must ostensibly reside in a ''noise-dominated'' regime to produce cluster distributions that match observations.

10. Summary and discussion

a. *Summary*

A two-dimensional stochastic model, part of a hierarchy based on vertically integrated moisture, condensate and WTG temperature equations, is introduced to reproduce the observed precipitation cluster size and power pdfs. The pdfs are characterized by a power law with slope ~−1.5 and a cutoff at large power or size. The degree of organization, quantified here by the value of the cutoff, is sensitive to the presence of moisture convergence–latent heating feedbacks that preferentially intensify the upper-level divergence over precipitating points, and weaken the divergence over nonprecipitating points. The positive feedbacks between moisture convergence and latent heating, temporal persistence in divergence, and spatial connectivity via lateral mixing process collectively shape the statistics of precipitation clusters. The lateral mixing is effectively represented by diffusion, but in the absence of explicit diffusion, other processes such rotational wind advection assume a similar function. Reductions in the stochastic forcing and increases in the moisture–radiative feedbacks yield aggregated clusters, comparable to those observed in cloud-permitting RCE simulations. The slope of the distribution is fairly robust in the parameter range explored in this study. The cutoff exhibits sensitivity to multiple model parameters, although it is independent of grid size, that is, it is a true physical scale. This cutoff sensitivity is captured using a metric that quantifies the likelihood of a precipitating pixel

emerging in the neighborhood of an existing precipitating pixel. This metric was inspired by apparent connections between a stochastic prototype called the stochastic branching process, and a mechanism that captures how precipitation clusters might grow in space. This branching process is also posited to explain why the observed slopes of the cluster distributions lie close to −1.5.

b. Relevance of the stochastic branching process

How strongly should we emphasize the connections between the SBP and the physics of convective organization? We use apparent analogies between the two systems to collapse the multiparameter dependence of a_L and c_L in our model, although the SBP helps capture variations in a_L better than in c_L. Strong connections between the two systems also suggest an explanation for the robustness of the cluster pdf slopes in the face of parameter perturbations in section 4, and their observed values (close to −1.5). The SBP thus appears to hold promise as a prototype for how tropical precipitating systems organize, but issues such as the lack of a direct analog for cluster decay in the SBP are worth future scrutiny. The mapping from physical model parameters to the SBP parameter (mean number of branches per generation) is also not obtained from first principles. A theory to directly connect the physical cutoff scales to the parameters of the moist processes remains desirable.

c. The emergence of the mesoscale

Tropical convective systems—excluding tropical cyclones—occupy a broad range of spatial scales. Even MCS (systems $>\sim 10^3$ km^2 in area) are not characterized a single distinguishing horizontal scale, but are commonly identified by their distinctive flow (Zipser 1977; Moncrieff 1992; Mapes and Houze 1995) and heating structures (Houze 1982; Schumacher et al. 2004). The interesting scale-related question for such systems, therefore, does not concern their typical size, but rather, their largest attainable size. In precipitation cluster size distributions, this quantity is closely related to a_L; precipitation clusters can exceed a_L in size, but do so with a probability that drops rapidly. Our model cluster size distribution, much like observed tropical clusters, has a scale-free range and a cutoff, a_L, that marks the length scale associated with the largest precipitation clusters. The cluster size cutoff a_L in our model is not controlled by any single process, but emerges from a set of constituent, interacting processes. Transferring our results to real tropical systems implies that the scale of large tropical systems is an emergent property with multiple controls—and that these controls can be condensed using a measure of neighbor interactions like λ_{nn}, from section 8. This implication about the emergent nature of a_L is consistent with studies linking a_L to "convective sustainability": a measure of environmental ability to support buoyant convective elements (Yuter and Houze 1998; Schumacher and Houze 2006). The nearest neighbor probability λ_{nn} subsumes information about convective sustainability, in addition to the strength of neighbor interactions. For example, increases in surface evaporation E lead to increased convective sustainability—by uniformly enhancing the likelihood of precipitation—and consequently, a_L; but so do increases in the efficiency of lateral mixing (increases in D_q). An interesting extension of our model would be to study the cluster statistics in the presence of planetary rotation and examine how a_L interacts with the Rossby deformation radius.

d. Interactive radiation and self-aggregation

The results from our simple model suggest that radiative effects of the water substance support—but are not the sole drivers of—convective organization. Our results also highlight the distinction between the *process* of interactive radiation and the *phenomenon* of self-aggregation. We find that self-aggregation (in the sense of radiatively driven separation between moist and dry regions) is absent in the noise-dominated regime that supports realistic cluster distributions, and only appears in a distinct regime dominated by strong radiative feedbacks. Unlike the observed cluster distributions, the clusters in the self-aggregated regime show preference for a horizontal scale—indicated by "peaks" in the cluster pdf—associated with the strength of the moisture–radiative feedbacks. This preferred scale in the cluster pdfs is likely related to the length scale of self-aggregation in CRMs (Yang 2018; Beucler and Cronin 2019), but these results must be verified in CRMs. Overall, we find that stochastic variability—supplied by the "multiscale potpourri of atmospheric circulation" (Bretherton and Khairoutdinov 2015)—and elementary moist physics are sufficient to reproduce the gross statistics of precipitation clusters.

e. Implications for climate models

Climate models can reproduce the observed precipitation cluster size and power distributions, with reasonable fidelity, though there are quantitative variations among them (QN17b). The connections with the branching probability and the efficacy of a measure like λ suggests that convective parameterizations that are influenced by neighbor communication (e.g., Mapes and Neale 2011; Bengtsson et al. 2013; Bengtsson and Körnich 2016) are steps in the right direction toward producing realistic statistics of convective organization. The role of temporally autocorrelated noise in our

model suggests that convective parameterization schemes with memory (Khouider et al. 2010; Goswami et al. 2017) could also improve the representation of convective organization. The use of λ can aid understanding of the more basic metrics for the cutoff in cluster area and power, a_L and c_L, which can in turn be used to assess model performance with respect to organized convection. Parameter perturbation experiments that track changes to these metrics could potentially be used to judge the relevance of convective organization to the mean climate (Bony et al. 2015). There are also large disagreements among climate models about future changes to extreme tropical precipitation (O'Gorman 2015), which are associated with mesoscale convection (Rossow et al. 2013). Parameters a_L and c_L could potentially help constrain this intermodel spread by acting as useful climate predictors in emergent constraints studies (Klein and Hall 2015). When compared to a_L, c_L is robust to rain thresholds and parameter perturbations, including α^{-1}—an important parameter in convective parameterization schemes. This property makes c_L, the cluster power cutoff, a more desirable measure of extreme events in climate models. Therefore, c_L serves as a suitable overall aggregate measure of moist processes involved in neighbor interactions, and may thus find use in measuring these interactions within climate model ensembles.

One of the documented consequences of global warming in climate models is the increase in the threshold value of moisture that triggers precipitation, that is, q_c (Sahany et al. 2014). In our model, a_L and c_L increase dramatically with q_c, implying an increase in the frequency of large, organized precipitating systems in a warmer world. This result is consistent with reports of increasingly disproportionate contributions from organized convection (QN17a,b; Tan et al. 2015b; Pendergrass et al. 2016) to future precipitation increases.

Acknowledgments. This research was supported in part by National Science Foundation Grant AGS-1540518 and by National Oceanic and Atmospheric Administration Grant NOAA17 NA18OAR4310280. This work was motivated in part by discussions with S. Stechmann and K. Quinn's doctoral thesis. Conversations with C. Martinez-Villalobos and J. Norris and a review by T. Cronin improved aspects of this study. A portion of this work was presented at the 99th American Meteorological Society Annual Meeting.

REFERENCES

Alstrøm, P., 1988: Mean-field exponents for self-organized critical phenomena. *Phys. Rev.*, **A38**, 4905–4906, https://doi.org/10.1103/PhysRevA.38.4905.

Arakawa, A., and V. R. Lamb, 1977: Computational design of the basic dynamical processes of the UCLA General Circulation Model. *General Circulation Models of the Atmosphere*, J. Chang, Ed., Methods in Computational Physics: Advances in Research and Applications, Vol. 17, Elsevier, 173–265, https://doi.org/10.1016/B978-0-12-460817-7.50009-4.

Arnold, N. P., and D. A. Randall, 2015: Global-scale convective aggregation: Implications for the Madden-Julian Oscillation. *J. Adv. Model. Earth Syst.*, **7**, 1499–1518, https://doi.org/10.1002/2015MS000498.

Athreya, K. B., and P. E. Ney, 2011: T. E. Harris and branching processes. *Ann. Probab.*, **39**, 429–434, https://doi.org/10.1214/10-AOP599.

Back, L. E., and C. S. Bretherton, 2006: Geographic variability in the export of moist static energy and vertical motion profiles in the tropical Pacific. *Geophys. Res. Lett.*, **33**, L17810, https://doi.org/10.1029/2006GL026672.

Bao, J., and S. C. Sherwood, 2019: The role of convective self-aggregation in extreme instantaneous versus daily precipitation. *J. Adv. Model. Earth Syst.*, **11**, 19–33, https://doi.org/10.1029/2018MS001503.

Bengtsson, L., and H. Körnich, 2016: Impact of a stochastic parametrization of cumulus convection, using cellular automata, in a mesoscale ensemble prediction system. *Quart. J. Roy. Meteor. Soc.*, **142**, 1150–1159, https://doi.org/10.1002/qj.2720.

——, M. Steinheimer, P. Bechtold, and J.-F. Geleyn, 2013: A stochastic parametrization for deep convection using cellular automata. *Quart. J. Roy. Meteor. Soc.*, **139**, 1533–1543, https://doi.org/10.1002/qj.2108.

Betts, A. K., 1986: A new convective adjustment scheme. Part I: Observational and theoretical basis. *Quart. J. Roy. Meteor. Soc.*, **112**, 677–691, https://doi.org/10.1002/QJ.49711247307.

——, and M. J. Miller, 1986: A new convective adjustment scheme. Part II: Single column tests using gate wave, BOMEX, ATEX and Arctic air-mass data sets. *Quart. J. Roy. Meteor. Soc.*, **112**, 693–709, https://doi.org/10.1002/QJ.49711247308.

Beucler, T., and T. W. Cronin, 2016: Moisture–radiative cooling instability. *J. Adv. Model. Earth Syst.*, **8**, 1620–1640, https://doi.org/10.1002/2016MS000763.

——, and ——, 2019: A budget for the size of convective self-aggregation. *Quart. J. Roy. Meteor. Soc.*, **145**, 947–966, https://doi.org/10.1002/QJ.3468.

Bony, S., and Coauthors, 2015: Clouds, circulation and climate sensitivity. *Nat. Geosci.*, **8**, 261–268, https://doi.org/10.1038/ngeo2398.

Bretherton, C. S., and M. F. Khairoutdinov, 2015: Convective self-aggregation feedbacks in near-global cloud-resolving simulations of an aquaplanet. *J. Adv. Model. Earth Syst.*, **7**, 1765–1787, https://doi.org/10.1002/2015MS000499.

——, P. N. Blossey, and M. Khairoutdinov, 2005: An energy-balance analysis of deep convective self-aggregation above uniform SST. *J. Atmos. Sci.*, **62**, 4273–4292, https://doi.org/10.1175/JAS3614.1.

Cahalan, R. F., and J. H. Joseph, 1989: Fractal statistics of cloud fields. *Mon. Wea. Rev.*, **117**, 261–272, https://doi.org/10.1175/1520-0493(1989)117<0261:FSOCF>2.0.CO;2.

Charney, J., 1947: The dynamics of long waves in a baroclinic westerly current. *J. Atmos. Sci.*, **4**, 136–162, https://doi.org/10.1175/1520-0469(1947)004<0136:TDOLWI>2.0.CO;2.

Chen, S. S., R. A. Houze Jr., and B. E. Mapes, 1996: Multiscale variability of deep convection in relation to large-scale circulation in TOGA COARE. *J. Atmos. Sci.*, **53**, 1380–1409, https://doi.org/10.1175/1520-0469(1996)053<1380:MVODCI>2.0.CO;2.

Cheng, W.-Y., D. Kim, and A. Rowe, 2018: Objective quantification of convective clustering observed during the AMIE/DYNAMO two-day rain episodes. *J. Geophys. Res. Atmos.*, **123**, 10 361–10 378, https://doi.org/10.1029/2018JD028497.

Chou, C., and J. D. Neelin, 2003: Mechanisms limiting the northward extent of the northern summer monsoons over North America, Asia, and Africa. *J. Climate*, **16**, 406–425, https://doi.org/10.1175/1520-0442(2003)016<0406:MLTNEO>2.0.CO;2.

——, and ——, 2004: Mechanisms of global warming impacts on regional tropical precipitation. *J. Climate*, **17**, 2688–2701, https://doi.org/10.1175/1520-0442(2004)017<2688:MOGWIO>2.0.CO;2.

——, ——, C.-A. Chen, and J.-Y. Tu, 2009: Evaluating the "rich-get-richer" mechanism in tropical precipitation change under global warming. *J. Climate*, **22**, 1982–2005, https://doi.org/10.1175/2008JCLI2471.1.

——, T.-C. Wu, and P.-H. Tan, 2013: Changes in gross moist stability in the tropics under global warming. *Climate Dyn.*, **41**, 2481–2496, https://doi.org/10.1007/s00382-013-1703-2.

Craig, G. C., and J. M. Mack, 2013: A coarsening model for self-organization of tropical convection. *J. Geophys. Res. Atmos.*, **118**, 8761–8769, https://doi.org/10.1002/JGRD.50674.

Ding, B., C. Li, M. Zhang, G. Lu, and F. Ji, 2014: Numerical analysis of percolation cluster size distribution in two-dimensional and three-dimensional lattices. *Eur. Phys. J. B*, **87**, 179, https://doi.org/10.1140/epjb/e2014-40996-4.

Eady, E. T., 1949: Long waves and cyclone waves. *Tellus*, **1**, 33–52, https://doi.org/10.3402/tellusa.v1i3.8507.

Eckart, C., 1948: An analysis of the stirring and mixing processes in compressible fluids. *J. Mar. Res.*, **7** (3), 265–275.

Emanuel, K., A. A. Wing, and E. M. Vincent, 2014: Radiative–convective instability. *J. Adv. Model. Earth Syst.*, **6**, 75–90, https://doi.org/10.1002/2013MS000270.

Feng, Z., S. Hagos, A. K. Rowe, C. D. Burleyson, M. N. Martini, and S. P. de Szoeke, 2015: Mechanisms of convective cloud organization by cold pools over tropical warm ocean during the AMIE/DYNAMO field campaign. *J. Adv. Model. Earth Syst.*, **7**, 357–381, https://doi.org/10.1002/2014MS000384.

Fovell, R. G., 2002: Upstream influence of numerically simulated squall-line storms. *Quart. J. Roy. Meteor. Soc.*, **128**, 893–912, https://doi.org/10.1256/0035900021643737.

——, G. L. Mullendore, and S.-H. Kim, 2006: Discrete propagation in numerically simulated nocturnal squall lines. *Mon. Wea. Rev.*, **134**, 3735–3752, https://doi.org/10.1175/MWR3268.1.

Gardiner, C. W., 2004: *Handbook of Stochastic Methods for Physics, Chemistry and the Natural Sciences*. 3rd ed. Springer Series in Synergetics, Vol. 13, Springer, 415 pp.

Goswami, B., B. Khouider, R. Phani, P. Mukhopadhyay, and A. Majda, 2017: Improved tropical modes of variability in the NCEP Climate Forecast System (version 2) via a stochastic multicloud model. *J. Atmos. Sci.*, **74**, 3339–3366, https://doi.org/10.1175/JAS-D-17-0113.1.

Harris, T. E., 1963: *The Theory of Branching Processes*. Die Grundlehren der Mathematischen Wissenschaften, Bd. 119, Springer, 230 pp.

Held, I. M., and A. Y. Hou, 1980: Nonlinear axially symmetric circulations in a nearly inviscid atmosphere. *J. Atmos. Sci.*, **37**, 515–533, https://doi.org/10.1175/1520-0469(1980)037<0515:NASCIA>2.0.CO;2.

——, and B. J. Soden, 2006: Robust responses of the hydrological cycle to global warming. *J. Climate*, **19**, 5686–5699, https://doi.org/10.1175/JCLI3990.1.

——, and M. Zhao, 2008: Horizontally homogeneous rotating radiative–convective equilibria at GCM resolution. *J. Atmos. Sci.*, **65**, 2003–2013, https://doi.org/10.1175/2007JAS2604.1.

Hottovy, S., and S. N. Stechmann, 2015: A spatiotemporal stochastic model for tropical precipitation and water vapor dynamics. *J. Atmos. Sci.*, **72**, 4721–4738, https://doi.org/10.1175/JAS-D-15-0119.1.

Houze, R. A., Jr., 1982: Cloud clusters and large-scale vertical motions in the tropics. *J. Meteor. Soc. Japan*, **60**, 396–410, https://doi.org/10.2151/JMSJ1965.60.1_396.

——, 1997: Stratiform precipitation in regions of convection: A meteorological paradox? *Bull. Amer. Meteor. Soc.*, **78**, 2179–2196, https://doi.org/10.1175/1520-0477(1997)078<2179:SPIROC>2.0.CO;2.

——, 2004: Mesoscale convective systems. *Rev. Geophys.*, **42**, RG4003, https://doi.org/10.1029/2004RG000150.

Huffman, G. J., and Coauthors, 2007: The TRMM Multisatellite Precipitation Analysis (TMPA): Quasi-global, multiyear, combined-sensor precipitation estimates at fine scales. *J. Hydrometeor.*, **8**, 38–55, https://doi.org/10.1175/JHM560.1.

Inoue, K., and L. E. Back, 2015: Gross moist stability assessment during TOGA COARE: Various interpretations of gross moist stability. *J. Atmos. Sci.*, **72**, 4148–4166, https://doi.org/10.1175/JAS-D-15-0092.1.

Jeevanjee, N., and D. M. Romps, 2013: Convective self-aggregation, cold pools, and domain size. *Geophys. Res. Lett.*, **40**, 994–998, https://doi.org/10.1002/grl.50204.

Johnson, R. H., 1984: Partitioning tropical heat and moisture budgets into cumulus and mesoscale components: Implications for cumulus parameterization. *Mon. Wea. Rev.*, **112**, 1590–1601, https://doi.org/10.1175/1520-0493(1984)112<1590:PTHAMB>2.0.CO;2.

Kendall, D. G., 1966: Branching processes since 1873. *J. London Math. Soc.*, **s1-41**, 385–406, https://doi.org/10.1112/JLMS/S1-41.1.385.

Khouider, B., 2014: A coarse grained stochastic multi-type particle interacting model for tropical convection: Nearest neighbour interactions. *Commun. Math. Sci.*, **12**, 1379–1407, https://doi.org/10.4310/CMS.2014.v12.n8.a1.

——, J. Biello, and A. J. Majda, 2010: A stochastic multicloud model for tropical convection. *Commun. Math. Sci.*, **8**, 187–216, https://doi.org/10.4310/CMS.2010.v8.n1.a10.

Klein, S. A., and A. Hall, 2015: Emergent constraints for cloud feedbacks. *Curr. Climate Change Rep.*, **1**, 276–287, https://doi.org/10.1007/s40641-015-0027-1.

Kuang, Z., 2012: Weakly forced mock Walker cells. *J. Atmos. Sci.*, **69**, 2759–2786, https://doi.org/10.1175/JAS-D-11-0307.1.

Lane, T. P., and F. Zhang, 2011: Coupling between gravity waves and tropical convection at mesoscales. *J. Atmos. Sci.*, **68**, 2582–2598, https://doi.org/10.1175/2011JAS3577.1.

Lin, Z., K. Bodová, and C. R. Doering, 2010: Models and measures of mixing and effective diffusion. arXiv, https://arxiv.org/abs/1011.1320.

López, R. E., 1978: Internal structure and development processes of c-scale aggregates of cumulus clouds. *Mon. Wea. Rev.*, **106**, 1488–1494, https://doi.org/10.1175/1520-0493(1978)106<1488:ISADPO>2.0.CO;2.

Machado, L. A. T., W. B. Rossow, R. L. Guedes, and A. W. Walker, 1998: Life cycle variations of mesoscale convective systems over the Americas. *Mon. Wea. Rev.*, **126**, 1630–1654, https://doi.org/10.1175/1520-0493(1998)126<1630:LCVOMC>2.0.CO;2.

Majda, A. J., and M. G. Shefter, 2001: Models for stratiform instability and convectively coupled waves. *J. Atmos. Sci.*, **58**,

1567–1584, https://doi.org/10.1175/1520-0469(2001)058<1567:MFSIAC>2.0.CO;2.

——, B. Khouider, and Y. Frenkel, 2015: Effects of rotation and mid-troposphere moisture on organized convection and convectively coupled gravity waves. *Climate Dyn.*, **44**, 937–960, https://doi.org/10.1007/s00382-014-2222-5.

Mapes, B. E., 1993: Gregarious tropical convection. *J. Atmos. Sci.*, **50**, 2026–2037, https://doi.org/10.1175/1520-0469(1993)050<2026:GTC>2.0.CO;2.

——, 2000: Convective inhibition, subgrid-scale triggering energy, and stratiform instability in a toy tropical wave model. *J. Atmos. Sci.*, **57**, 1515–1535, https://doi.org/10.1175/1520-0469(2000)057<1515:CISSTE>2.0.CO;2.

——, and R. A. Houze, 1995: Diabatic divergence profiles in western Pacific mesoscale convective systems. *J. Atmos. Sci.*, **52**, 1807–1828, https://doi.org/10.1175/1520-0469(1995)052<1807:DDPIWP>2.0.CO;2.

——, and R. Neale, 2011: Parameterizing convective organization to escape the entrainment dilemma. *J. Adv. Model. Earth Syst.*, **3**, M06004, https://doi.org/10.1029/2011MS000042.

Martinez-Villalobos, C., and J. D. Neelin, 2018: Shifts in precipitation accumulation extremes during the warm season over the United States. *Geophys. Res. Lett.*, **45**, 8586–8595, https://doi.org/10.1029/2018GL078465.

Matsuno, T., 1966: Quasi-geostrophic motions in the equatorial area. *J. Meteor. Soc. Japan*, **44**, 25–43, https://doi.org/10.2151/JMSJ1965.44.1_25.

Merlis, T. M., W. Zhou, I. M. Held, and M. Zhao, 2016: Surface temperature dependence of tropical cyclone-permitting simulations in a spherical model with uniform thermal forcing. *Geophys. Res. Lett.*, **43**, 2859–2865, https://doi.org/10.1002/2016GL067730.

Mohr, K. I., and E. J. Zipser, 1996: Mesoscale convective systems defined by their 85-GHz ice scattering signature: Size and intensity comparison over tropical oceans and continents. *Mon. Wea. Rev.*, **124**, 2417–2437, https://doi.org/10.1175/1520-0493(1996)124<2417:MCSDBT>2.0.CO;2.

Moncrieff, M. W., 1992: Organized convective systems: Archetypal dynamical models, mass and momentum flux theory, and parametrization. *Quart. J. Roy. Meteor. Soc.*, **118**, 819–850, https://doi.org/10.1002/qj.49711850703.

Muller, C. J., and I. M. Held, 2012: Detailed investigation of the self-aggregation of convection in cloud-resolving simulations. *J. Atmos. Sci.*, **69**, 2551–2565, https://doi.org/10.1175/JAS-D-11-0257.1.

——, and S. Bony, 2015: What favors convective aggregation and why? *Geophys. Res. Lett.*, **42**, 5626–5634, https://doi.org/10.1002/2015GL064260.

Neelin, J. D., and I. M. Held, 1987: Modeling tropical convergence based on the moist static energy budget. *Mon. Wea. Rev.*, **115**, 3–12, https://doi.org/10.1175/1520-0493(1987)115<0003:MTCBOT>2.0.CO;2.

——, and N. Zeng, 2000: A quasi-equilibrium tropical circulation model—Formulation. *J. Atmos. Sci.*, **57**, 1741–1766, https://doi.org/10.1175/1520-0469(2000)057<1741:AQETCM>2.0.CO;2.

——, O. Peters, and K. Hales, 2009: The transition to strong convection. *J. Atmos. Sci.*, **66**, 2367–2384, https://doi.org/10.1175/2009JAS2962.1.

——, S. Sahany, S. N. Stechmann, and D. N. Bernstein, 2017: Global warming precipitation accumulation increases above the current-climate cutoff scale. *Proc. Natl. Acad. Sci. USA*, **114**, 1258–1263, https://doi.org/10.1073/pnas.1615333114.

Neggers, R. A. J., H. J. J. Jonker, and A. P. Siebesma, 2003: Size statistics of cumulus cloud populations in large-eddy simulations. *J. Atmos. Sci.*, **60**, 1060–1074, https://doi.org/10.1175/1520-0469(2003)60<1060:SSOCCP>2.0.CO;2.

Nolan, D. S., E. D. Rappin, and K. A. Emanuel, 2007: Tropical cyclogenesis sensitivity to environmental parameters in radiative–convective equilibrium. *Quart. J. Roy. Meteor. Soc.*, **133**, 2085–2107, https://doi.org/10.1002/qj.170.

O'Gorman, P. A., 2015: Precipitation extremes under climate change. *Curr. Climate Change Rep.*, **1**, 49–59, https://doi.org/10.1007/s40641-015-0009-3.

Pendergrass, A. G., K. A. Reed, and B. Medeiros, 2016: The link between extreme precipitation and convective organization in a warming climate: Global radiative–convective equilibrium simulations. *Geophys. Res. Lett.*, **43**, 11 445–11 452, https://doi.org/10.1002/2016GL071285.

Peters, O., J. D. Neelin, and S. W. Nesbitt, 2009: Mesoscale convective systems and critical clusters. *J. Atmos. Sci.*, **66**, 2913–2924, https://doi.org/10.1175/2008JAS2761.1.

——, A. Deluca, A. Corral, J. D. Neelin, and C. E. Holloway, 2010: Universality of rain event size distributions. *J. Stat. Mech.: Theory Exp.*, **2010**, P11030, https://doi.org/10.1088/1742-5468/2010/11/P11030.

——, K. Christensen, and J. D. Neelin, 2012: Rainfall and dragon-kings. *Eur. Phys. J. Spec. Top.*, **205**, 147–158, https://doi.org/10.1140/epjst/e2012-01567-5.

Pritchard, M. S., and C. S. Bretherton, 2014: Causal evidence that rotational moisture advection is critical to the superparameterized Madden–Julian oscillation. *J. Atmos. Sci.*, **71**, 800–815, https://doi.org/10.1175/JAS-D-13-0119.1.

Quinn, K. M., and J. D. Neelin, 2017a: Distributions of tropical precipitation cluster power and their changes under global warming. Part I: Observational baseline and comparison to a high-resolution atmospheric model. *J. Climate*, **30**, 8033–8044, https://doi.org/10.1175/JCLI-D-16-0683.1.

——, and ——, 2017b: Distributions of tropical precipitation cluster power and their changes under global warming. Part II: Long-term time dependence in coupled model intercomparison project phase 5 models. *J. Climate*, **30**, 8045–8059, https://doi.org/10.1175/JCLI-D-16-0701.1.

Raymond, D. J., S. L. Sessions, A. H. Sobel, and Ž. Fuchs, 2009: The mechanics of gross moist stability. *J. Adv. Model. Earth Syst.*, **1**, 9, https://doi.org/10.3894/JAMES.2009.1.9.

Rossow, W. B., A. Mekonnen, C. Pearl, and W. Goncalves, 2013: Tropical precipitation extremes. *J. Climate*, **26**, 1457–1466, https://doi.org/10.1175/JCLI-D-11-00725.1.

Sahany, S., J. D. Neelin, K. Hales, and R. B. Neale, 2014: Deep convective transition characteristics in the community climate system model and changes under global warming. *J. Climate*, **27**, 9214–9232, https://doi.org/10.1175/JCLI-D-13-00747.1.

Schumacher, C., and R. A. Houze, 2006: Stratiform precipitation production over sub-Saharan Africa and the tropical east Atlantic as observed by TRMM. *Quart. J. Roy. Meteor. Soc.*, **132**, 2235–2255, https://doi.org/10.1256/qj.05.121.

——, ——, and I. Kraucunas, 2004: The tropical dynamical response to latent heating estimates derived from the TRMM Precipitation Radar. *J. Atmos. Sci.*, **61**, 1341–1358, https://doi.org/10.1175/1520-0469(2004)061<1341:TTDRTL>2.0.CO;2.

Schumacher, R. S., and R. H. Johnson, 2005: Organization and environmental properties of extreme-rain-producing mesoscale convective systems. *Mon. Wea. Rev.*, **133**, 961–976, https://doi.org/10.1175/MWR2899.1.

Shi, X., and C. S. Bretherton, 2014: Large-scale character of an atmosphere in rotating radiative–convective equilibrium. *J. Adv. Model. Earth Syst.*, **6**, 616–629, https://doi.org/10.1002/2014MS000342.

Sobel, A. H., and C. S. Bretherton, 2000: Modeling tropical precipitation in a single column. *J. Climate*, **13**, 4378–4392, https://doi.org/10.1175/1520-0442(2000)013<4378:MTPIAS>2.0.CO;2.

——, J. Nilsson, and L. M. Polvani, 2001: The weak temperature gradient approximation and balanced tropical moisture waves. *J. Atmos. Sci.*, **58**, 3650–3665, https://doi.org/10.1175/1520-0469(2001)058<3650:TWTGAA>2.0.CO;2.

Sornette, D., 2006: *Critical Phenomena in Natural Sciences: Chaos, Fractals, Selforganization and Disorder: Concepts and Tools*. Springer, 528 pp.

Stauffer, D., and A. Aharony, 1992: *Introduction to Percolation Theory*. 2nd ed. Taylor & Francis, 192 pp.

Stechmann, S. N., and J. D. Neelin, 2011: A stochastic model for the transition to strong convection. *J. Atmos. Sci.*, **68**, 2955–2970, https://doi.org/10.1175/JAS-D-11-028.1.

——, and ——, 2014: First-passage-time prototypes for precipitation statistics. *J. Atmos. Sci.*, **71**, 3269–3291, https://doi.org/10.1175/JAS-D-13-0268.1.

Tan, J., C. Jakob, and T. P. Lane, 2015a: The consequences of a local approach in statistical models of convection on its large-scale coherence. *J. Geophys. Res. Atmos.*, **120**, 931–944, https://doi.org/10.1002/2014JD022680.

——, ——, W. B. Rossow, and G. Tselioudis, 2015b: Increases in tropical rainfall driven by changes in frequency of organized deep convection. *Nature*, **519**, 451–454, https://doi.org/10.1038/nature14339.

Teo, C.-K., H.-N. Huynh, T.-Y. Koh, K. K. W. Cheung, B. Legras, L. Y. Chew, and L. Norford, 2017: The universal scaling characteristics of tropical oceanic rain clusters. *J. Geophys. Res. Atmos.*, **122**, 5582–5599, https://doi.org/10.1002/2016JD025921.

Tompkins, A. M., 2001: Organization of tropical convection in low vertical wind shears: The role of cold pools. *J. Atmos. Sci.*, **58**, 1650–1672, https://doi.org/10.1175/1520-0469(2001)058<1650:OOTCIL>2.0.CO;2.

Torri, G., Z. Kuang, and Y. Tian, 2015: Mechanisms for convection triggering by cold pools. *Geophys. Res. Lett.*, **42**, 1943–1950, https://doi.org/10.1002/2015GL063227.

Traxl, D., N. Boers, A. Rheinwalt, B. Goswami, and J. Kurths, 2016: The size distribution of spatiotemporal extreme rainfall clusters around the globe. *Geophys. Res. Lett.*, **43**, 9939–9947, https://doi.org/10.1002/2016GL070692.

Tulich, S. N., and B. E. Mapes, 2008: Multiscale convective wave disturbances in the tropics: Insights from a two-dimensional cloud-resolving model. *J. Atmos. Sci.*, **65**, 140–155, https://doi.org/10.1175/2007JAS2353.1.

Vere-Jones, D., 1977: Statistical theories of crack propagation. *J. Int. Assoc. Math. Geol.*, **9**, 455–481, https://doi.org/10.1007/BF02100959.

Villermaux, E., 2019: Mixing versus stirring. *Annu. Rev. Fluid Mech.*, **51**, 245–273, https://doi.org/10.1146/annurev-fluid-010518-040306.

Watson, H. W., and F. Galton, 1875: On the probability of the extinction of families. *J. Anthropol. Inst. G. B. Irel.*, **4**, 138–144, https://doi.org/10.2307/2841222.

Welander, P., 1955: Studies on the general development of motion in a two-dimensional, ideal fluid. *Tellus*, **7**, 141–156, https://doi.org/10.3402/tellusa.v7i2.8797.

Wing, A. A., and K. A. Emanuel, 2014: Physical mechanisms controlling self-aggregation of convection in idealized numerical modeling simulations. *J. Adv. Model. Earth Syst.*, **6**, 59–74, https://doi.org/10.1002/2013MS000269.

——, and T. W. Cronin, 2016: Self-aggregation of convection in long channel geometry. *Quart. J. Roy. Meteor. Soc.*, **142**, 1–15, https://doi.org/10.1002/qj.2628.

——, K. Emanuel, C. E. Holloway, and C. Muller, 2018: Convective self-aggregation in numerical simulations: A review. *Shallow Clouds, Water Vapor, Circulation, and Climate Sensitivity*, R. Pincus et al., Eds., Springer, 1–25, https://doi.org/10.1007/978-3-319-77273-8_1.

Wood, R., and P. R. Field, 2011: The distribution of cloud horizontal sizes. *J. Climate*, **24**, 4800–4816, https://doi.org/10.1175/2011JCLI4056.1.

Yang, D., 2018: Boundary layer height and buoyancy determine the horizontal scale of convective self-aggregation. *J. Atmos. Sci.*, **75**, 469–478, https://doi.org/10.1175/JAS-D-17-0150.1.

Yano, J.-I., S. Mulet, and M. Bonazzola, 2009: Tropical large-scale circulations: asymptotically non-divergent? *Tellus*, **61A**, 417–427, https://doi.org/10.1111/j.1600-0870.2009.00397.x.

Yu, J.-Y., C. Chou, and J. D. Neelin, 1998: Estimating the gross moist stability of the tropical atmosphere. *J. Atmos. Sci.*, **55**, 1354–1372, https://doi.org/10.1175/1520-0469(1998)055<1354:ETGMSO>2.0.CO;2.

Yuan, J., and R. A. Houze, 2010: Global variability of mesoscale convective system anvil structure from a-train satellite data. *J. Climate*, **23**, 5864–5888, https://doi.org/10.1175/2010JCLI3671.1.

Yuter, S. E., and R. A. Houze Jr., 1998: The natural variability of precipitating clouds over the western Pacific warm pool. *Quart. J. Roy. Meteor. Soc.*, **124**, 53–99, https://doi.org/10.1002/qj.49712454504.

Zeng, N., J. D. Neelin, and C. Chou, 2000: A quasi-equilibrium tropical circulation model—Implementation and simulation. *J. Atmos. Sci.*, **57**, 1767–1796, https://doi.org/10.1175/1520-0469(2000)057<1767:AQETCM>2.0.CO;2.

Zipser, E. J., 1977: Mesoscale and convective–scale downdrafts as distinct components of squall-line structure. *Mon. Wea. Rev.*, **105**, 1568–1589, https://doi.org/10.1175/1520-0493(1977)105<1568:MACDAD>2.0.CO;2.

Zuidema, P., G. Torri, C. Muller, and A. Chandra, 2017: A survey of precipitation-induced atmospheric cold pools over oceans and their interactions with the larger-scale environment. *Surv. Geophys.*, **38**, 1283–1305, https://doi.org/10.1007/s10712-017-9447-x.